Investigating mass transfer coefficients in lean methane combustion reaction through the morphological and geometric analysis of structured open cell foam catalysts

(Article begins on next page)

Investigating mass transfer coefficients in lean methane combustion reaction through the morphological and geometric analysis of structured open cell foam catalysts

Carmen W. Moncada Quintero [a,*], Hernan G. Mazzei [a], Marion Servel [b], Frédéric Augier [b], Yacine Haroun [b], Jean-François Joly [b], Stefania Specchia [a,*]

[a] *Politecnico di Torino, Department of Applied Science and Technology, Corso Duca degli Abruzzi 24, I-10129 Torino, Italy*
[b] *IFP Energies Nouvelles, Établissement de Lyon, Rond-point de l'échangeur de Solaize, BP 3, F-69360 Solaize, France*

ABSTRACT

In this work, we characterized ceramic open cell foams made of zirconia, silicon carbide and alumina of different nominal pore densities (30–45 ppi) using X-ray computed microtomography. This technique allowed the comprehensive and quantitative extraction of morphological and geometrical characteristics of the structures (pore size, strut diameter and length, node diameter, open porosity and specific geometrical surface area). An empirical model was proposed to determine the specific surface area from parameters easily accessible with standard laboratory equipment. Moreover, lean CH_4 combustion tests were performed on ceramic foams coated with PdO/Co_3O_4 at 3 wt%. Mass transfer coefficients of the foams were measured by monitoring the oxidation reaction under diffusional control conditions. We derived a dimensionless correlation of the type $Sh = A \bullet Re^m \bullet Sc^{1/3}$. Finally, the pressure drop across the foams as a function of surface velocity was evaluated and compared with various experimental data and models available in the literature.

1. Introduction

In recent years, open cell foams (OCFs) have become one of the most attractive structures for a wide variety of industrial applications in the field of chemical engineering for process intensification (Aguirre et al., 2020; Bracconi et al., 2020), as well as in other engineering applications (Banhart, 2001; Banhart and Weaire, 2011; Grosse et al., 2009). OCFs are irregular cellular materials made of interconnected solid struts that give rise to a continuous three-dimensional network, which enclose empty regions called cells (Bracconi et al., 2017; Buciuman and Kraushaar-Czarnetzki, 2003; Große et al., 2008; Inayat et al., 2011, 2016). This network leads to a highly porous structure that provides a flow pathway through the open windows that communicates with neighboring cells, as shown in Fig. 1A. Foams are also characterized by a unique combination of physical properties such as high rigidity, light-weight, high specific surface area, and permeability (Della Torre et al., 2016; Kumar et al., 2015; Razza et al., 2016; Scheffler and Colombo, 2005), offering clear advantages over classical fixed or packed bed reactors (Ambrosetti et al., 2017; Sinn et al., 2021; Zalucky et al., 2015).

Depending on their composition, metallic or ceramic, OCFs have attracted interest in the design of compact heat exchangers (Haack et al., 2001; Ozmat et al., 2004; Vazifeshenas et al., 2020) as well as structured catalysts (Aguirre et al., 2020; Buciuman and Kraushaar-Czarnetzki, 2003; Specchia et al., 2017), burner heads (Gao et al., 2012; Ortona et al., 2010), fuel cell bipolar flow plates (Baroutaji et al., 2017; Tseng et al., 2012) and as structured packaging for the process intensification of reactors and columns (Balzarotti et al., 2020; Cristiani et al., 2012; Ercolino et al., 2017b; Groppi et al., 2007; Ho et al., 2019; Incera Garrido et al., 2008; Lu et al., 1998; Moncada Quintero et al., 2021a, 2021b, 2022). Several authors have reported a remarkable enhancement in catalytic performance when using foams as catalyst supports instead of operating in classical packed bed reactors or even in other types of substrates such as honeycombs and monoliths (Balzarotti et al., 2020; Ciambelli et al., 2010; Della Torre et al., 2016; Ercolino et al., 2017a). The reason for this can be primarily attributed to the enhanced flow mixing created by the tortuous paths, which improves mass and heat transfer properties. Consequently, this leads to lower pressure drops in comparison to fixed beds. Both metallic and ceramic OCFs can be

---

* Corresponding authors.
E-mail addresses: carmen.moncada@polito.it (C.W. Moncada Quintero), stefania.specchia@polito.it (S. Specchia).

fabricated using methods as replication or direct foaming, where the choice of one material or the other depends on the structure's application (Buciuman and Kraushaar-Czarnetzki, 2003; García-Moreno, 2016; Richardson et al., 2003, 2000; Scheffler and Colombo, 2005; Twigg and Richardson, 2002).

Recently, we studied OCFs and monoliths made of ceramic material as catalytic supports for highly endothermic and exothermic reactions (Ashraf et al., 2018; Ercolino et al., 2017c, 2017a; Italiano et al., 2018; Moncada Quintero et al., 2021a, 2021b). We found that both foams and monoliths showed excellent catalyst adhesion and a significant improvement in catalytic activity and mass transfer per unit volume. Such advantage results in a lower amount of noble metal to be loaded on the surface, which determines a cost reduction in the reactor design. Moreover, we also demonstrated that an increase of the catalyst loading (as mg of catalyst per cm^2 of OCF) drives to a greater dominance of the internal mass transfer resistance and limited residence time to complete the reaction (Moncada Quintero et al., 2021b). Moreover, a correlation for mass transfer in OCFs at low Reynolds number was proposed. The data were collected from lean CH_4 combustion tests carried out under gas/solid diffusional control in zirconia foams of 30 ppi. However, although the derived expression fitted well with our experimental data, the correlation was limited to a narrow range of pore diameters (Moncada Quintero et al., 2021b). Clearly, in structures such as OCFs, the hydrodynamic and transport properties are strongly influenced by their distinct morphology and geometric attributes, encompassing pore size, strut thickness, porosity, specific surface area, and other related factors. These properties not only allow to characterize the structure, but also to obtain a detailed analysis of the fluid-dynamic processes occurring within the foam network. In particular, the specific surface area of the foams is one of the most important factors that influence both momentum, heat and mass transfer and pressure drop across structures, which are extremely relevant features for reactor design. Since the unit cell of foams commonly resembles a polyhedron with pentagonal or hexagonal faces bounding a spherical-looking interior space, various authors have proposed different models to represent the open cell foam structures (Bracconi et al., 2017; Grosse et al., 2009; Inayat et al., 2011, 2016; Incera Garrido et al., 2008; Richardson et al., 2003). Lord Kelvin proposed the first deterministic model in 1887 (Thomson (Lord Kelvin) (1887)). This model was based on a tetrakaidecahedron cell (or commonly known as Kelvin cell) composed of fourteen faces (eight hexagonal and six quadrilaterals) and twenty-four vertices, as shown in Fig. 1B. Kelvin suggested the tetrakaidecahedron cell as a packing pattern and stated that the shape of the cell was capable of dividing space into identical units of equal volume with minimal surface energy (Favata, 2012; Podio-Guidugli and Favata, 2014; Thomson (Lord Kelvin) (1887)). Later, Weaire and Phelan (Weaire and Phelan, 1994) proposed an improved model of the Kelvin cell consisting of eight cells, six tetrakaidecahedra and two pentagonal dodecahedra. The structure proposed by the authors showed a surface area reduction of 0.3% with respect to the Kelvin structure. Nevertheless, the adoption of an anisotropic periodic cell structure showed an unusual mechanical compatibility due to the lack of randomness which is found in real foams. Habisreuther at al. (Habisreuther et al., 2009) and Lucci et al. (Lucci et al., 2014) varied the vertices positions of the ordered Kelvin multicellular structure using vectors with stochastic directions and values. Other researchers based their study on random models using Voronoi tessellation. This model requires initial seed points, which are generated by randomly packing spheres of cell diameter size through a discrete element method (Bracconi et al., 2017; Maliaris and Michailidis, 2014). Once the spheres are settled, the centers are extracted and imported into the Voronoi algorithm, thus generating the foam skeleton. Such model has proven to be able to adequately reproduce foams consisting of closed and open cells, allowing the generation of large virtual cellular structures following a predefined cell size distribution, cell arrangement and cross-section strut distribution law (Gibson and Ashby, 1988; Kraynik et al., 2003; Randrianalisoa et al., 2002). However, some authors have pointed out that the number of struts per vertex of the structures generated by Voronoi tessellation is higher than that of real foam structures, and the structural parameters of the foams reconstructed by Voronoi tessellation are different from those of real foams (Habisreuther et al., 2009; Wejrzanowski et al., 2013). Fig. 1B shows the most common theoretical models for representing foams.

As technology has advanced, imaging techniques that recreate the three-dimensional structure of materials have become one of the fundamental tools in the study and inspection of the properties of solids. Particularly, X-ray computed micro-tomography (micro-CT) is considered one of the most advanced methods in the field of non-destructive testing, indispensable in the characterization of morphological properties of structures (Moncada Quintero et al., 2021b; Montminy et al., 2004; Papetti et al., 2018; Schmierer et al., 2016). The technique is based on the non-invasive and non-destructive inspection of the internal structure of a solid with a spatial resolution at the micron level that allows the construction of a three-dimensional model from two-dimensional cross-sectional image slices. It also provides a detailed exploration of the morphological and architectural parameters characteristic of the material, thus leading to a modeling study of the material structure (Inayat et al., 2011; Kim et al., 2014; Ou et al., 2017; Petit et al., 2017). The prediction of properties from microstructural information requires an accurate quantitative description of the material (Inayat et al., 2016).
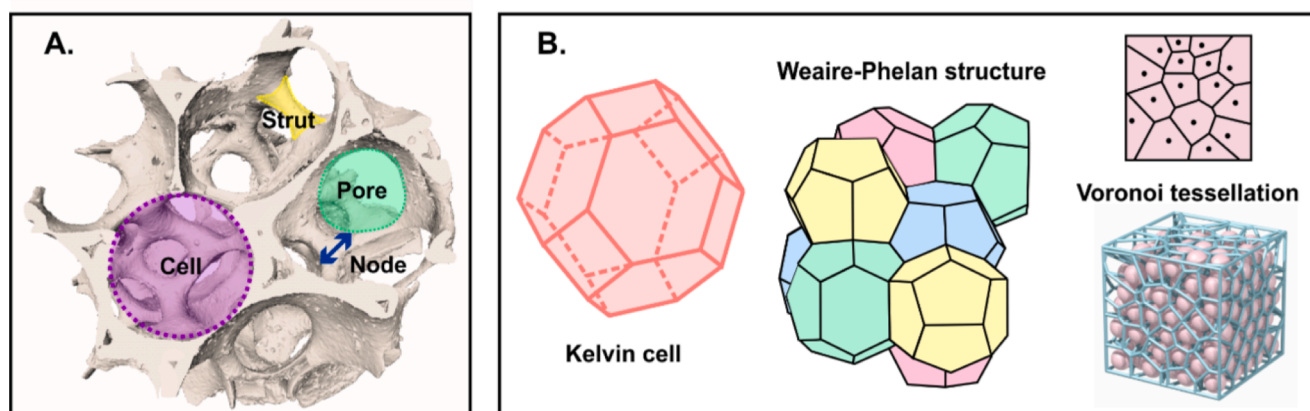

Fig. 1. Morphological characteristic parameters of OCFs (A), Kelvin unit cell, Weaire-Phelan structure and typical Voronoi tessellation used to represent the foam structure (B).

In the present contribution, we conducted a comprehensive characterization of commercially available OCFs made of zirconia (Zir), silicon carbide (SiC), and alumina (Alu) at different nominal pore densities (30 and 45 pores per inch, ppi). While the literature reports correlations for SiC and Alu OCFs, up to now there are no correlations available for Zir OCFs. Utilizing X-ray micro-tomography techniques and image analysis, we extracted crucial structural information such as pore size, strut thickness, porosity, and specific surface area of different types of OCFs (Zir, SiC, and Alu). In the existing literature, most studies on open-cell ceramic foams primarily focus on analyzing pore and strut diameter. In this study, we not only address these characteristic dimensions but also provide measurements of node dimension, length, and strut angle. In fact, these parameters are crucial for modeling purposes, providing the chance to better represent the real 3D structure of the investigated OCFs. Furthermore, we evaluated the suitability and validity of several correlations reported in the literature for estimating the specific geometrical surface area of ceramic foams by comparing them with our experimental results. Additionally, based solely on our experimental findings, we derived an empirical model that accurately determines the specific surface area using parameters easily accessible with standard laboratory equipment. This empirical model accounts for the three types of OCFs, including Zir OCFs for the first time. To further stress the practical implications of our research, we conducted lean CH_4 combustion tests were also performed on 3 wt% PdO/Co_3O_4 coated ceramic foams by varying the volumetric flow rate and inlet methane concentration. Analyzing the data, we discussed the controlling regimes (kinetic or diffusional control) across the temperature range of 100–700 °C. To assess mass transfer properties, we measured mass transfer coefficients by monitoring oxidation reactions under diffusion-controlled conditions, deriving a dimensionless correlation ($Sh = A \cdot Re^m \cdot Sc^{\frac{1}{3}}$) applicable to a wide range of foam geometrical properties. Finally, we evaluated the pressure drop across OCFs as a function of superficial velocity, comparing our findings with experimental data and models from the literature.

2. Experimental section

2.1. Ceramic open cell foams (OCFs)

In this study, ceramic OCFs made of zirconia (Vukopor® HT, labelled as Zir), silicon carbide (Vukopor® S, labelled as SiC), and alumina (Vukopor® A, labelled as Alu) with nominal pore densities of 30 and 45 ppi each were analyzed. Foams were manufactured by Lanik S.r.o. ("Lanik Foam Ceramics," n.d.) (Czech Republic) and supplied in cylindrical shapes with dimensions of 40 mm or 9 mm in diameter and 30 mm in length. The fabrication process of the structures adopted by the company is based on the polymeric foam replication technique, in which OCFs are obtained as positive images of the template. Basically, this technique consists of infiltrating the ceramic slurry (containing Al_2O_3, SiC, ZrO_2, etc.) into the polymeric foam, removing the excess slurry, drying and then burning the polymeric template (Richardson et al., 2000; Scheffler and Colombo, 2005; Twigg and Richardson, 2007, 2002). Thus, once the template is vaporized, the ceramic particles sinter together giving rise to a ceramic replica or positive image ceramic foam. Table S1 in the *Supporting Information* reports the chemical composition of the ceramic OCFs studied in this work, as provided by the manufacturer ("Lanik Foam Ceramics," n.d.).

2.2. X-ray computed tomography characterization of the OCFs

The structural characterization and 3D internal reconstruction of the foams was carried out using the non-destructive X-ray computed microtomography technique (micro-CT). Micro-CT scans were performed with an EasyTom (RX Solutions, France) system equipped with a 150/160 kV micro focus X-ray tube and a Varian plat panel detector. The principle of

tomographic image acquisition consisted of directing X-rays at an object from multiple orientations and measuring the decrease in intensity along a series of linear trajectories (rotational axis) (Richard Ketcham, n. d.).Figure S1 shows a schematic representation of the micro-CT device. The scan procedure can be briefly described as follows: i) the foam sample is placed on a rotating stage between the X-ray source and the detector, ii) a source transmits X-rays with a certain intensity, where part of the radiation is absorbed, part is scattered and the rest penetrates through the specimen, iii) the amount of X-rays attenuated by the sample is recorded by the detector, iv) the foam sample is then rotated 360° to transmit the rays from all possible directions with an angular rotation interval of 0.25°and exposure time of 2 s, resulting in 1440 images per sample and lastly, v) a computer algorithm captures the data of each discrete part producing a 2D projection/scanned image and the CT slices are reconstructed by software creating the 3D volumetric rendering of the foams.

Samples of size 40x30 mm were analyzed using two X-ray generators to estimate the characteristic internal dimensions of the foams: i) a 150 kV microfocus X-ray tube, with X-ray power set at 80 kV, current of 142 μA and pixel size of 22 μm and ii) a 160 kV microfocus X-ray tube, with X-ray power at 100 kV, current of 50 μA and pixel size of 1.70 and 5 μm. Smaller foam cylinders (9 mm × 30 mm) were also examined to determine the open porosity and geometric surface area of the macroporous solid using a microfocus X-ray tube set at 70 kV and 200 μA. The aforementioned parameters were selected to maximize the available spatial resolution within the system, while ensuring that the entire foam volume remained within the field of view. The resulting voxel size was 14 μm per pixel. This value ensures an optimal trade-off between precision and computational cost, allowing for the scanning of each strut with more than 50 voxels in the transverse direction (Bracconi et al., 2019; Ou et al., 2017; Plumb et al., 2018). For all measurements, an aluminum filter was used to selectively attenuate or block lower energy photons during X-ray imaging.

2.3. Image processing

After image acquisition, the micro-CT slices were reconstructed by filtered back projection algorithm using the RX Solutions software integrated into the device. The tomograms obtained were then exported as a 16-bit grayscale image stack. Subsequently, a three-dimensional (3D) model was reconstructed using Avizo Thermo Fisher Scientific software version 2019.1 for further image processing (visualization, correction, segmentation, and data quantification) based on the principles of morphological image analysis (Lacroix et al., 2007; Moreira et al., 2004). Micro-CT sub-volumes ($1006 \times 1006 \times 736$ voxels) were selected to remove uninteresting regions from the original micro-CT image. Afterwards, a Gaussian filter (Kernel size factor of 2) was employed to blur and reduce the noise introduced during the image acquisition/transmission step (Große et al., 2008). This filter allowed smoothing the region of interest while preserving edges and corners of the solid structure. Finally, a segmentation process was applied to transform the original image volume into a binary volume. Basically, the ceramic solid phase (low-signal region) and the gas phase contained within the void cells (high-signal region) were distinguished by converting the grayscale micro-CT data into a binary format using the adaptive histogram technique developed by Otsu (Otsu, 1979). This method is based on an automatic global thresholding algorithm focused on the maximization of separability in gray level classes (Inayat et al., 2011; Kim et al., 2014; Neethirajan et al., 2006; Otsu, 1979; Ridler and Calvard, 1978). After assigning each voxel to either the fluid or solid phase, it was possible to extract the information from the 3D reconstruction of the structure. The resulting virtual slices exhibited a voxel size of $14 \times 14 \times 14 \ \mu m^3$. At this point, the images were ready for data processing and analysis, leading to the complete characterization of the OCFs. In addition to Avizo, the free software FijiImageJ was used to extract information such as mean strut length (l_s), mean pore and strut diameter (d_p, d_s), etc. The

characterization of geometric surface area (S_{ga}) and open porosity (ε_o) was performed using Avizo. It is worth highlighting that before applying the thresholding, a volume of interest (VOI, in our case cylindrical) containing the sample to be analyzed was selected. Therefore, once the material of interest within the VOI was segmented, the binary volume could be processed. Briefly, the process consisted of 1) applying the 'Label Analysis' operator on the image data; 2) assigning the original data as an 'Intensity Image' in the specific port of the module; and 3) selecting the fundamental measurements in the 'Measure port' of the 'Label Analysis' operator, followed by subsequent processing (Ou et al., 2017).

In order to determine the geometric surface area and open porosity of the structures, the following equations were employed within the 'Measure port':

$$S_{ga} = \frac{Area3D}{Volume3D} \tag{1}$$

$$\varepsilon_o = 1 - \frac{Volume3D}{CYL} \tag{2}$$

where *Area*3D, *Volume*3D, and *CYL* are basic measurements computed within the 'Measure port' operator. *Area*3D corresponds to the surface area of the macroporous solid, *Volume*3D corresponds to the volume of the macroporous solid, and *CYL* corresponds to the volume of the cylinder containing the analyzed sample (VOI). All these measurements were acquired in voxels. The surface area is directly quantified in 3D using the marching cubes algorithm included in the software's quantification module (Lindblad, 2005; Lorensen and Cline, 1987). This algorithm also allowed for the generation of a triangular surface mesh, which was saved in a stereolithographic file (.stl) to expand our future investigation on OCFs in terms of modeling and finite element analysis (Béchet et al., 2002). On the other hand, when examining OCFs, two types of porosity are generally considered: open porosity (ε_o), which refers solely to the empty space existing between the strut networks of the foam, and total porosity (ε_t), which also includes microscopic pores (cavities) present within the foam's skeleton. However, since the micro-CT resolution employed in this study (14 μm) was smaller than the size of these microscopic cavities in the ceramic material, only the open porosity was characterized. Thus, to facilitate the determination of ε_o and prevent the CT software from recognizing some cavities (micro- and mesopores) within the foam struts as part of the open porosity, the 'Watershed' operator was first applied to perform preliminary segmentation. Subsequently, a morphological closing operation was carried out using the 'Closing' operator (which utilizes elements known as kernels in Avizo) (Ou et al., 2017). This operation allowed filling the strut porosity (ε_s) and avoiding interference during the analysis.

2.4. Preparation of OCF structured catalysts

Ahead of use, all structures were thoroughly washed in order to remove possible impurities present on the substrate surface such as grease, dirt, dust, stains, fingerprints, etc. For this purpose, the foams were sonicated at room temperature in an acetone–water solution (50:50 v/v) for 30 min and dried in an oven at 140 °C for 60 min. Once the structures were cleaned, the PdO/Co$_3$O$_4$ catalyst coating was carried out in the following two consecutive steps (Moncada Quintero et al., 2021a, 2021b): i) Co$_3$O$_4$ deposition via solution combustion synthesis and ii) wetness impregnation of the PdO active phase. Briefly, a 3 M aqueous solution of cobalt nitrate (as oxidizing agent) and glycine (as fuel) with a fuel/oxidizer ratio of 0.25 to the stoichiometric amount was prepared. The mixture was stirred with a magnetic stirrer until the salts were completely dissolved. Afterwards, each OCF was carefully immersed in the precursor solution for about 3 min and the excess solution was removed by a flow of compressed air. The wet OCFs were then placed in a muffle furnace at 250 °C for 15 min to allow ignition of the combustion reaction. The coating operation was repeated several

times till the desired amount of ~ 200 mg Co$_3$O$_4$ was reached. Lastly, the so-prepared OCFs were calcined at 600 °C for 4 h in static air. After coating the OCFs with cobalt oxide, a 3 wt% of PdO was deposited via wet impregnation, using an aqueous solution of palladium nitrate that contained the exact amount of PdO based on the deposited carrier mass. The procedure consisted in dipping each coated OCF in the aqueous solution ensuring that the whole OCF was completely covered. Drying the wet OCF in a muffle set at 140 °C for 1 h for water evaporation concluded the impregnation step. The operation was repeated several times up to the complete consumption of the palladium nitrate solution. Finally, the PdO/Co$_3$O$_4$ coated OCFs were calcined at 600 °C for 4 h.

2.5. Catalytic activity

All structures (Alu-OCF, SiC-OCF and Zir-OCF of 30 and 45 ppi) coated with 3 wt% PdO/Co$_3$O$_4$ were tested for the lean methane oxidation in a lab-scale straight quartz reactor (10 mm inner diameter) placed into an electrical furnace controlled by a PID system. A thin film of vermiculite was used to wrap each catalytic foam in order to avoid channeling phenomena and minimize heat dispersion to the external environment. The structure was then positioned at the center of the reactor and the furnace was heated up to 700 °C with an N$_2$ flow rate of 0.1 NL min^{-1} and a heating rate of 10 °C min^{-1}. Once the set temperature was reached, the reactor was fed with the reactant gas mixture composed of CH$_4$, O$_2$ and N$_2$ at WHSV of 30, 60 and 90 NL h^{-1} g$_{cat}^{-1}$ (with volumetric flow rates equivalent to 0.1, 0.2 and 0.3 NL min^{-1}, respectively). To assure the repeatability of the experimental data, three runs per OCFs were performed with CH$_4$ inlet concentrations of 0.5 or 1 vol%, 4.0 or 8.0 vol% O$_2$ in N$_2$, keeping the O$_2$/CH$_4$ molar ratio constant at 8 to ensure lean conditions. Once steady state conditions were reached at 700 °C, the reactor was cooled to room temperature with a ramp of 5 °C min^{-1} and the dry gas concentrations at the reactor outlet were monitored as a function of temperature. For this purpose, an ABB analyzer equipped with an Uras 14 NDIR module for CO/CO$_2$/CH$_4$ and a Magnos 106 paramagnetic module for O$_2$ was employed. The water vapor generated from the combustion reaction was removed before entering the analyzer in a condenser set at 3 °C. The reaction temperature was monitored with a K-type thermocouple placed a few mm inside the inlet side of the OCF. This temperature was used for evaluation of the relevant physicochemical properties (gas viscosity, density, and diffusivity).

2.6. Pressure drop measurements

Gas flow hydrodynamics in OCFs plays a crucial role on the performance of processes such as filtration, adsorption and heterogeneous catalysis. Here, pressure drop across the foams (samples of 9 mm × 30 mm dimensions) was measured using a differential manometer TM 265–5 (Techmark) with the range of 0–500 Pa (accuracy = 0.1 Pa, sensibility = 0.01 Pa) at superficial velocities (u) ranging from 0.1 to 4 m s^{-1}. Before introducing the specimen at the center of the reactor, each OCF was wrapped with a thin film of vermiculite to avoid gas channeling at the foam/reactors' walls boundary. A mass flow controller (Brooks Instrument) was employed to supply the nitrogen flow rate (100–800 NmL min^{-1}) at room temperature. Forchheimer-extended Darcy model validated on OCFs was used to estimate the theoretical pressure drop per unit length (Bhattacharya et al., 2002; Boomsma et al., 2003; Hamadouche et al., 2016), according to the following equation:

$$\frac{\Delta P}{L} = a \cdot u + b \cdot u^2 \quad \text{or} \quad \frac{\Delta P}{L} = \frac{\mu}{k_1} \cdot u + \frac{\rho}{k_2} \cdot u^2 \tag{3}$$

where ΔP is the pressure drop, L is the measured foam length, u is the superficial velocity, μ is the dynamic viscosity of N$_2$, ρ is the density of N$_2$, a and b are the constants that represent the viscous resistance and the interfacial resistance and k_1 and k_2 are the viscous and inertial permeability parameters, respectively.

3. Results and discussion

3.1. Characteristic dimensions

Pore, strut, and node dimensions (d_p, d_s, l_s, d_n) were extracted directly from the 2D micro-CT images. In order to estimate the pore diameter (d_p), we first accurately evaluated the area of each pore (cross-sectional area of the void space) using the FijiImageJ software, then the diameter of an equivalent circle was determined (Fig. 2.**A**). As reported in our previous work (Moncada Quintero et al., 2021a), the circular pore shape assumption can be perfectly adopted for the analysis of foams as catalytic supports, even if the structures present mostly oval pores. As for the strut, because during the manufacturing process the ceramic precursor slurry is deposited mostly at the nodes instead of being homogeneously distributed along the length, the strut exhibits a variable cross-section with diameter values that reach a maximum at the intersections (nodes) and a minimum at the center of its length. We measured the diameter of the strut (d_s) in the middle of the strut length (l_s), and the node diameter (d_n) at the junction between the strut and the node (as shown in Fig. 2.**A** and **2.B**) using Fiji ImageJ (Incera Garrido et al., 2008; Lacroix et al., 2007). In addition, to gain a better understanding of the foam geometry, the angle between struts of all ceramic structures was also evaluated. More than 500 measurements were made for each characteristic dimension of the foams.

Fig. 3 (A.1/2 for Alu_30/Alu_45; B.1/2 for SiC_30/SiC_45; C.1/2 for Zir_30/Zir_45) shows the 2D image slices extracted from the micro-CT reconstruction for all the OCFs studied. It can be clearly observed that for all three ceramic materials, the increase in nominal pore density from 30 to 45 ppi leads to a much more compact structure due to the higher number of cells and hence struts per unit volume present in the foam. In fact, the increment of ppi caused a decrease in size of the characteristic morphological properties, since the higher the number of pores per linear inch, the smaller the cell size (as observed in Fig. 3 D/E/F/G/H). Interestingly at both ppi values, the zirconia foam exhibited larger morphological properties compared to the alumina and silicon carbide foams. For example, at 45 ppi, the Zir_45 foam shows an increase in pore size of 53 and 48 % with respect to the SiC_45 and Alu_45 foams, respectively. On the other hand, the SiC foam showed the lowest dimensions in terms of strut length and pore diameter at both ppi studied. Table S2 in the *Supporting Information* lists the min/max, average values and standard deviations of the pore/node/strut diameters, and strut length and strut-to-strut angle for all the OCFs analyzed. The slight deviations could be due to the method of analysis of the tomographic and microscopic images as well as to the method of fabrication of the foams applied by each manufacturer. As far as the strut-to-strut angle is concerned (α_{ss}), the mean values ranged between 115.6 and 118° (see Fig. 3**H**), being slightly higher than the theoretical angle reached at thermodynamic equilibrium in liquid foams, according to Plateau's laws (Plateau, 1873). These deviations have also been reported in the literature for polyurethane foams and the difference with respect to the theoretical rule was attributed to the fact that polymeric foams are not perfectly equilibrium structures, since they freeze before they can reach such a state (Montminy et al., 2004). Besides, the differences can also be attributed to the different shape stresses that can exist in the real foam systems (Montminy et al., 2004). For comparison, we plotted in Fig. 4**A** the mean values of node diameter vs. strut diameter obtained experimentally in this work with those reported in the literature on ceramic foams. Clearly, there is a linear correlation between d_n and d_s (Fig. 4**B**) and the values obtained here are in line with those reported previously by different authors on foams made of Al_2O_3 (Groppi et al., 2007; Incera Garrido et al., 2008; Twigg and Richardson, 2002), SiC (Lacroix et al., 2007; Ou et al., 2017) and SiSiC (Hernandez Camacho et al., 2019).

It is worth mentioning that in our previous work (Moncada Quintero et al., 2021b), we studied a 30 ppi Zir OCF as a support for a catalyst in the process of catalytic combustion of methane in lean conditions. Specifically, we studied the influence of the catalyst's loading on the reaction. The foams used were characterized by micro-CT. The difference between the values reported in the previous work with those obtained in this work could be due to the variability of the foam skeleton during the manufacturing process. Since in our previous work the pore and strut diameters of the Zir_30 foam were analyzed with specimens of smaller dimensions with respect to those studied in this section (40 mm × 30 mm), a narrower range of pores and thus, of strut, was covered. In fact, as we will discuss in the following sections, when analyzing the smaller cylindrical samples (9 mm × 30 mm), similar values of open porosity and geometric surface area were obtained.

Moreover, the pore size of OCFs is conventionally estimated by counting the number of pores per linear inch (usually denoted as ppi), referred to this paper as nominal pore density. Nevertheless, such a definition is rather confusing since in some studies the pore is usually the entire section of a cell, while in others it is a window (Ambrosetti et al., 2017; Inayat et al., 2011, 2016; Incera Garrido et al., 2008; Lacroix et al., 2007; Richardson et al., 2000; Schmierer et al., 2016; Twigg and Richardson, 2002). A cell represents a 3D volume, but the ppi reduces this volume to a linear measurement of the non-defined pore. Furthermore, this pore density, commonly used by foams' manufacturers, does
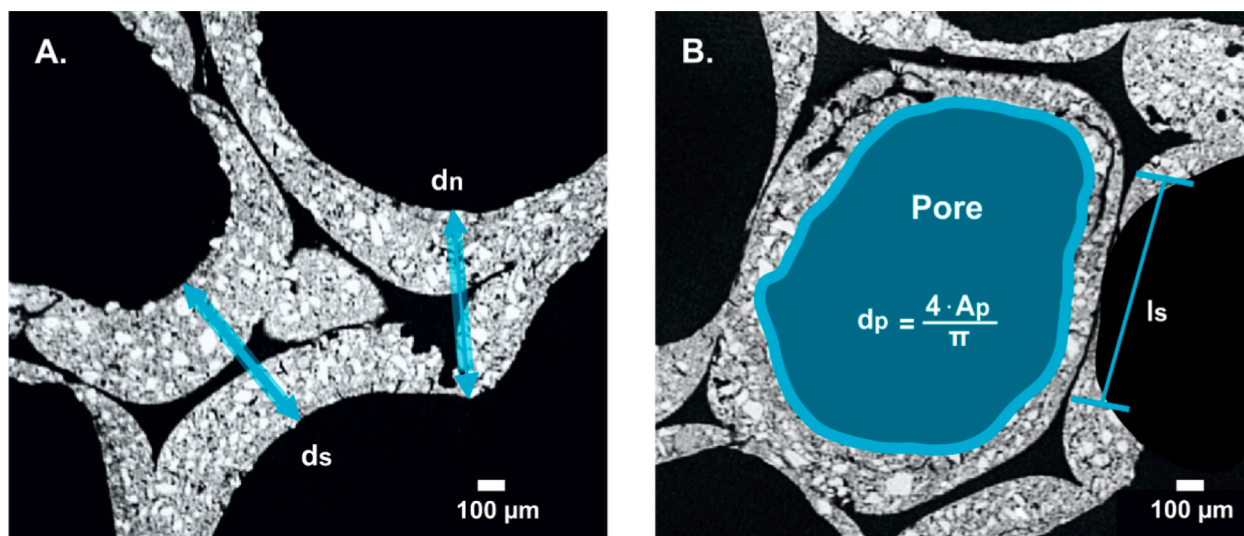

Fig. 2. Evaluation of node diameter, pore diameter, and strut length / diameter (pixel size of 5 μm).
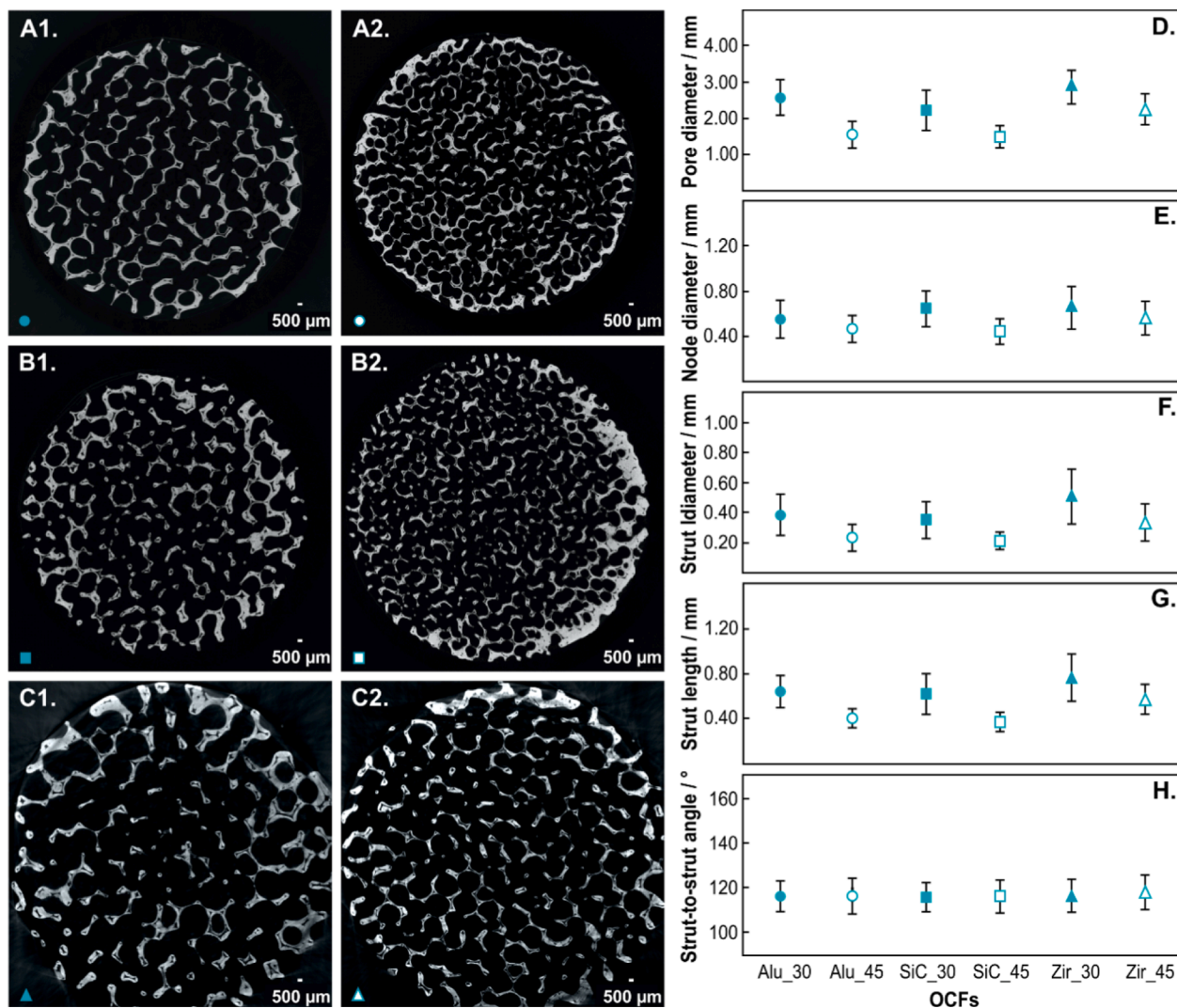
Fig. 3. 2D reconstructed CT slices (pixel size of 22 μm) for Alu_30/Alu_45 (A1/A2), SiC_30/SiC_45 (B1/B2), Zir_30/Zir_45 (C1/C2) and the mean and standard deviation of pore diameter (D), node diameter (E), strut diameter (F), strut length (G), and strut-to-strut angle (H) measured for all OCFs studied.
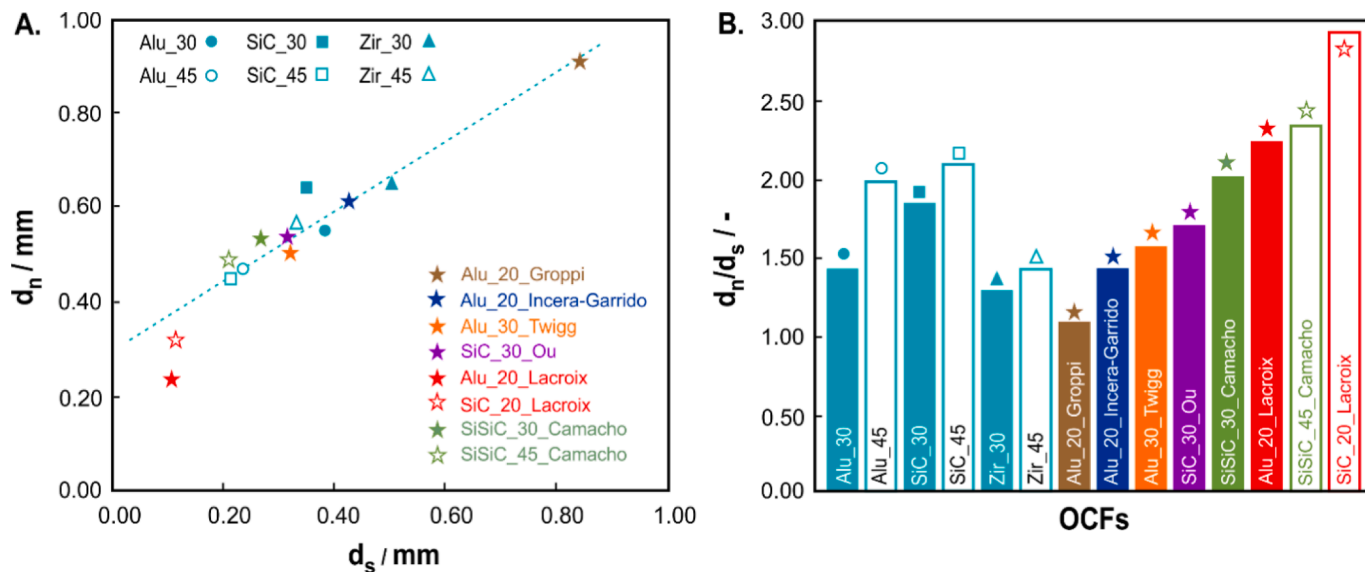

Fig. 4. Relationship between the node diameter and the strut diameter for Alu_30/Alu_45, SiC_30/SiC_45, Zir_30/Zir_45 and different OCFs from the open literature (A), and d_n/d_s ratio for all the OCFs examined (B).

not provide a precise measurement, but it merely represents a range of cell or pore sizes. Generally, the reference scale of foams changes according to each manufacturer, thus a foam defined as 80 ppi by one manufacturer could be defined as 110 ppi by another ("Visiocell® | Recticel Flexible Foams," n.d.). However, some authors still use the nominal ppi value in the determination of the pore size and as a modeling parameter (Mancin et al., 2013, 2010).

Another point worth noting is the presence of microporous walls (cavities) within the foam skeleton (Fig. 5**A**). This micro-porosity is commonly referred to as "strut porosity". It is originated during the manufacturing process (Grosse et al., 2009; Incera Garrido et al., 2008; Kumar, 2015; Richardson et al., 2000; Twigg and Richardson, 2007). Since most commercial foams, including those studied in this work are manufactured using the replication technique, the OCFs are obtained as positive images of the burned polymer templates giving rise to hollow struts with internal void volume. Such porosity can be avoided by using other manufacturing techniques such as direct foaming, which can result in fully dense solid skeletons but with much more closed cells (Ahmad et al., 2014; Mao, 2018; Zheng et al., 2020). A further aspect observed in the foam skeleton is the presence of dense grains along the microporous walls (Fig. 5**C**). These defects could be due to the various steps of the replication process, such as the preparation of ceramic slurry, the grain size of the ceramic particles, the dispersion of stabilizers or wetting agents, the viscosity, etc. (Ahmad et al., 2014; Liang et al., 2019; Mao, 2018). On the other hand, all the foams showed a circular strut cross-section shape (as shown in Fig. 5**B**).

3.2. Porosity

Several authors have reported that OCFs manufactured using the replication method are characterized by three types of porosity: i) open porosity (ε_o), ii) strut porosity (ε_s), and iii) total porosity (ε_t) (Bracconi et al., 2019; Grosse et al., 2009; Große et al., 2008; Inayat et al., 2011, 2016). Open porosity or also called hydrodynamic porosity refers to the void volume space present between the strut networks of the foam, which is fluid-dynamically relevant. The strut porosity, also called internal porosity, is the fraction of void present in the ceramic foam skeleton that originates from the manufacturing process, which is fluid-dynamically irrelevant. The total porosity is the combination of open and strut porosity, which can be expressed as follows:

$$\varepsilon_t = \varepsilon_o + \varepsilon_s \tag{4}$$

Fig. 6 shows a fragment of the strut (Fig. 6.**A**) and a zoom of the skeleton (Fig. 6.**B**) of the Zir_30 foam. Clearly, Fig. 6 reveals the presence of a micro-porosity within the structure. Since fluid access and even catalyst deposition inside the micro-pores are quite difficult, the hydrodynamic study of OCFs usually neglects the strut porosity. In fact, some authors have characterized the total and open porosity of foams using techniques such as helium pycnometry (Italiano et al., 2018) and mercury intrusion porosimetry (Bracconi et al., 2019; Grosse et al.,

2009; Inayat et al., 2011). They have concluded that the difference of such porosity values, due to the presence of any internal strut cavities was lower than 5 %.

Since the micro-CT technique does not allow access to the internal voids of the foam skeleton at an adequate resolution scale, only the macro-porosity of the OCFs was evaluated in this work. As mentioned in the *Experimental Section*, to determine the open porosity and avoid interference during micro-CT analysis caused by any cavity present within the strut foams (strut porosity), morphological operations of filling were applied (Ghazi et al., 2020; Ou et al., 2017), as shown in Fig. 7. Once the 3D image was reconstructed, a cylinder volume was analyzed and the measured open porosity ($\varepsilon_{o,m}$) was determined as:

$$\varepsilon_{o,m} = 1 - \frac{v_f}{v_c} \tag{5}$$

where v_f is the macro-porous solid volume and v_c is the analyzed cylinder volume.

Table 1 lists the nominal and measured (by micro-CT) porosity values of all ceramic OCFs studied. As observed, the difference between the value of nominal and estimated open porosities is below 5%. Furthermore, it is clear that the higher pore density the lower the void space of the macro-porous solid, which is in line with the measured open porosity values. However, such aspect cannot be evidenced in the porosity values supplied by the manufacturer, as they report only one open porosity value per ceramic material. On the other hand, it is important to highlight the influence of ε_o on the strut cross section. As we mentioned in the previous section, the circular cross section was mostly observed in all the ceramic OCFs studied in this work. Several authors have reported that the shape of the strut cross section in the foam skeleton depends directly on the material's open porosity (Calmidi and Mahajan, 1999; Huu et al., 2009; Inayat et al., 2011; Lacroix et al., 2007; Schmierer et al., 2016). Bhattacharya et al. (Bhattacharya et al., 2002) studied metal fiber foams made of aluminum alloy with porosities between 0.85 and 0.97. They concluded that the cross section of the strut changes from circular to triangular when the porosity reaches a value of 0.935. At porosities above 0.935, the cross section transforms into a concave triangular shape. Huu et al. (Huu et al., 2009) reported that the change of cross section from circular to triangular occurs at porosities of about 0.9. The authors concluded that such a phenomenon was valid in both ceramic and metal OCFs. However, they did not demonstrate experimental evidence of such a statement in ceramic OCFs. Later, Lacroix et al. (Lacroix et al., 2007) investigated ceramic OCFs made of β-SiC with porosities between 0.76 and 0.92. They reported the presence of a concave triangular shape at porosities above 0.9. Nevertheless, the porosity boundary where the triangular strut changes to concave has not yet been identified. Inayat et al. (Inayat et al., 2011) focused their study on the morphological properties of ceramic OCFs based on sintered silicon carbide with porosities below 0.9. The authors concluded that for open porosities lower than 0.9, the ceramic OCFs show circular cross section. All these studies mentioned above are in line with those
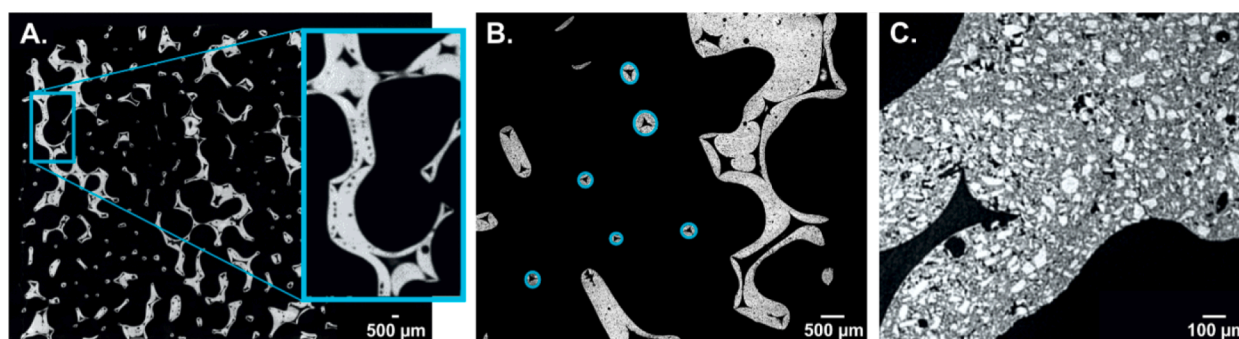

Fig. 5. 2D slices obtained by micro-CT with a pixel size of 5 μm: Foam micro-porosity (A. Alu_30), circular strut cross section (B. Alu_30) and dense grains along the micro-porous walls (C. SiC_30).
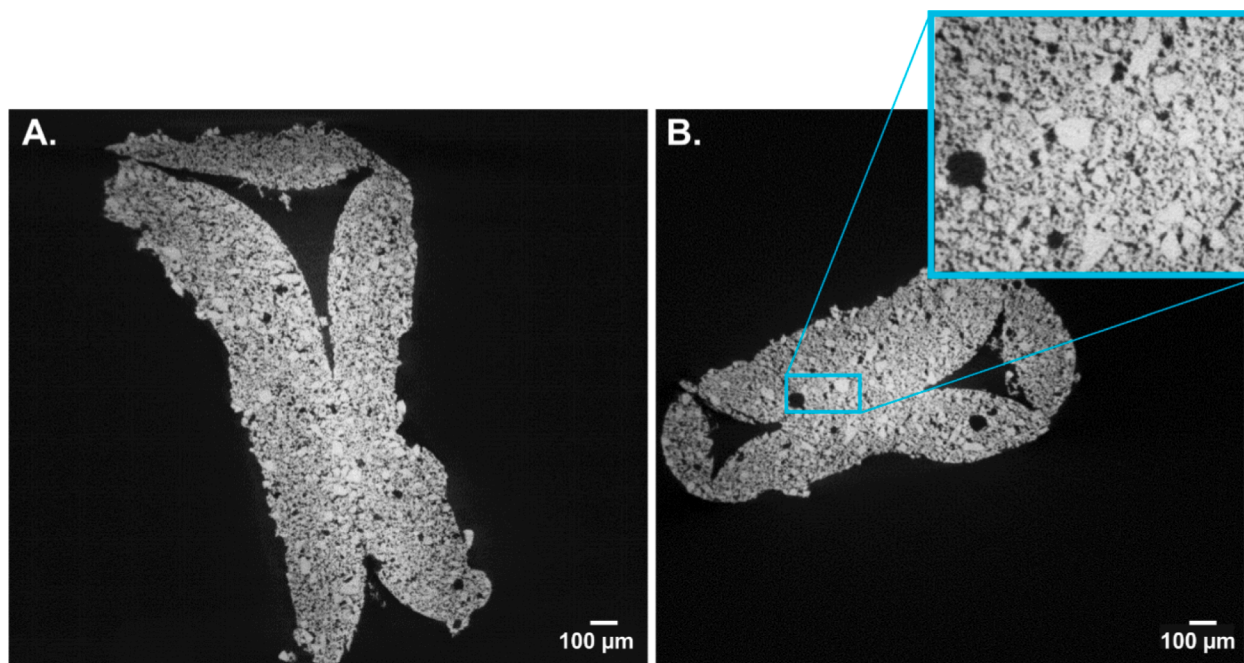
Fig. 6. 2D slices obtained by micro-CT with a pixel size of 1.7 μm: Fragment of the strut (A) and a magnification (B) of the Zir_30 foam skeleton.
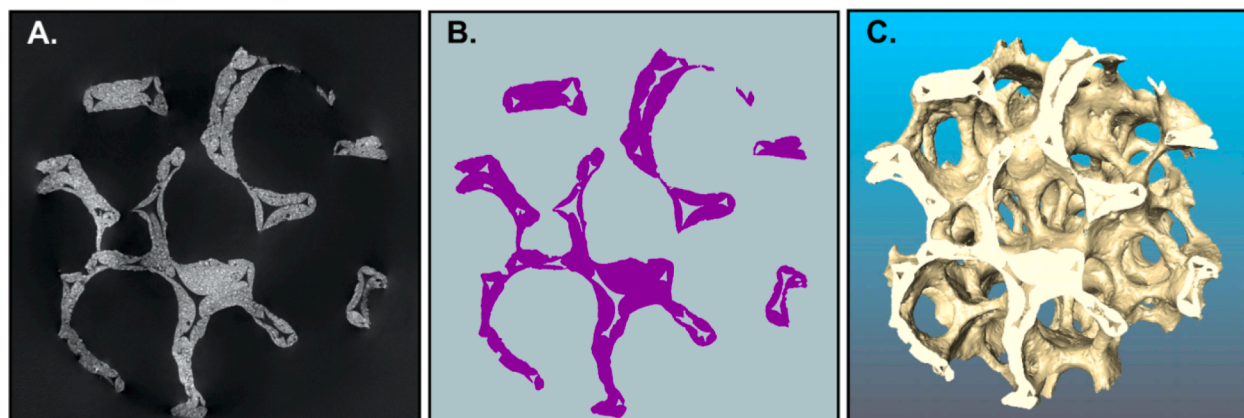

Fig. 7. (A) Raw gray scale micro-CT data of SiC_30, (B) after grayscale-based thresholding according to the method of Otsu (Otsu, 1979) and subsequent filling of the strut pores (closing operation in Avizo), (C) 3D reconstruction of the OCF.

Table 1
Nominal ($\varepsilon_{o,n}$) and measured ($\varepsilon_{o,m}$) open porosities, measured specific geometrical surface areas ($S_{ga,m}$) of all ceramic OCFs investigated (30 and 45 ppi).

foam	$\varepsilon_{o,n}$	$\varepsilon_{o,m}$	$S_{ga,m}$ [m^{-1}]
Alu_30	0.82	0.82	996.02
Alu_45		0.80	1480.85
SiC_30	0.82	0.79	899.90
SiC_45		0.78	1504.24
Zir_30	0.84	0.86	1092.15
Zir_45		0.84	1397.47

obtained in this work, where the three ceramic OCFs (Zir, Alu, and SiC) at open porosities in the range 0.78–0.86 showed a circular hollow strut cross section.

3.3. Specific surface area

The specific geometric surface area of OCFs is one of the most relevant properties for mass, heat, and momentum transfer, influencing the reaction rate in heterogeneous catalysis (Bernard et al., 2021), as well as being a key input parameter for the modeling of pressure drop across the structure (Mirdrikvand et al., 2020). It is defined as the total external surface area of the struts per unit geometric volume, assuming that all struts have a perfectly smooth surface. However, the material may have a rough surface and possess a porosity (cavities) within the hollow strut, as in the case of the ceramic OCFs studied in this work. Therefore, conventional methods such as nitrogen physisorption isotherms cannot be used to experimentally measure the specific surface area, since it leads to an overestimation of the parameter. Because of this fact, volume imaging techniques such as micro-CT play a fundamental role in the determination of the specific geometric surface area. We estimated the surface area of ceramic OCFs by analyzing micro-CT images of the samples using smaller specimens (9 mm × 30 mm in diameter and length, respectively) in order to reduce the computational efforts during data processing (Poryles et al., 2020).

The third column of Table 1 lists the specific surface area values of all the foams studies. As expected, the increase in pore density leads to a higher specific surface area due to the increase in the number of strut per

unit volume. Interestingly, at lower pore density the Zir OCF showed a higher specific geometric surface area with respect to Alu and SiC OCFs. However, as the pore density increased from 30 to 45 ppi, Alu and SiC OCFs showed a higher compactness (higher number of strut/solid phase per unit volume) in their structure compared to Zir OCF (see Fig. 3 from **A1** to **C2**), which led to higher specific surface areas for Alu and SiC OCFs with respect to the Zir one.

In order to compare the experimental values of specific surface area obtained here, we reviewed some literature-derived correlations developed as a function of open porosity, which take into account the cross section of the strut. Since the surface area/volume ratio changes with varying strut cross section, this may have a strong impact on the overall geometrical surface area. In the literature, different post-processing packages for foam tomography have been developed to reconstruct a three-dimensional representation of the structure and extract the relevant geometrical information (Montminy et al., 2004; Vicente et al., 2006). The uncertainty associated with the experimental assessment of specific surface area in OCFs using imaging techniques is linked not only to image resolution (voxel size), which can reach up to 15% (Kuhlmann et al., 2022; Schmierer and Razani, 2006), but also to the 3D reconstruction methodology of the structures and the image post-processing phase (Nyström et al., 2002). Therefore, we evaluate the validity and suitability of different correlations presented in literature for circular strut cross sections (based on both periodic unit cell assembly and empirical formulations) with the experimental specific surface area data obtained in this work. The related equations are reported in Table 2 and discussed below.

Lacroix et al. (Lacroix et al., 2007) used the cubic cell model originally proposed by Lu et al. (Lu et al., 1998) to derive a correlation of the specific geometric surface. This model considers the foam struts as cylindrical ligaments that are connected three-dimensionally giving rise to a regular cubic lattice. Later, Garrido et al. (Incera Garrido et al., 2008) proposed an empirical correlation in ceramic foams with porosities lower than 0.82. The authors introduced a dimensionless geometrical parameter (m) that allowed them to adjust their experimental values. On the other hand, Grosse et al. (Grosse et al., 2009) used the Weaire-Phelan structure to model their ceramic foams. Since their experimental results deviated from the theoretical model, they developed a semi-empirical correlation by fitting data while essentially maintaining the Weaire-Phelan model. Later, Lucci et. al. (Lucci et al., 2014) presented a model based on the stacking of regular Kelvin cells (TKKD model). They used the theoretical model to determine the specific surface area, and then compared them with a series of parametric CAD reconstructions of foams at different porosity and cell diameters. Since the theoretical model overestimated the values obtained at low porosities, they derived a correlation that permitted them to adjust the geometrical results. Recently, Ambrosetti et al. (Ambrosetti et al., 2017) developed a geometrical model of OCFs based on a Kelvin cell as a unitary periodic unit. This model was derived under purely analytical considerations

assuming that the shape of the strut was circular. The authors compared their results with a wide variety of foams of different porosity obtaining a good fit of the experimental results.

Fig. 8 highlights that the models based on the Kelvin cell provide a much closer approximation to the experimental values obtained. Particularly, the correlations derived by Lucci et. al. (Lucci et al., 2014) and Ambrosetti et al. (Ambrosetti et al., 2017) showed a deviation lower than 25 %, fitting our experimental data to a good extent. Similarly, the empirical correlation derived by Incera Garrido et al. (Incera Garrido et al., 2008) showed an error of 18 % for foams with porosity lower than 0.82, while increasing the porosity to 0.86, the deviation from our experimental results increased to 22 %. On the other hand, the equation derived by Lacroix et al. (Lacroix et al., 2007) overestimates the specific surface area values, while the Weaire-Phelan model deviates by approximately 53 % from our experimental values.

Thus, we developed an empirical model based on the geometric surface areas, pore diameters and open porosities estimated using our micro-CT by fitting parameters to experimental values, resulting in a good correlation of the geometric characteristics of ceramic OCFs with circular strut cross-sections (Fig. 8).

The equation we derived can be expressed as:

$$S_{ga} = \frac{2.688 \cdot \varepsilon_o^{-0.82}}{d_p + d_s} \tag{6}$$

More details on how this correlation has been derived are available in Figure S2 and related text of the *Supplementing Information*. We underline that this empirical correlation is valid for OCFs with porosity in the range 78–86 %, derived from OCFs of Alu, SiC, and Zir. To our knowlegde, in the literature there are no availability of data related to zirconia OCFs. As appreciable from Fig. 8, our correlation estimates the specific surface area of OCFs of different nature and porosity with an average error below 12%. Consequently its validity for OCFs different from these commercial ones, must be verified.

3.4. Mass transfer correlation for OCFs

In one of our previous work, we have derived an empirical correlation to estimate the mass transfer coefficients at low Reynolds number (Moncada Quintero et al., 2021b). The expression was obtained by performing lean CH_4 oxidation in Zir OCFs of 30 ppi coated with different PdO/Co_3O_4 catalyst loadings (6.1, 8.2, and 13.7 mg_{cat} cm^{-2}_{OCF}) under external diffusion-controlled conditions. The catalyst layer deposited on the Zir 30 ppi OCFs was assumed to be uniformly distributed on the inner walls of the foam pore, thus the corresponding average thicknesses were of 30.3, 41.1, and 68.5 μm, respectively. From that study, it was observed that the thicker the deposited catalyst layer, the higher the values of the mass transfer coefficients. This was explained due to the reduction of the pore size, and hence, of the cross-sectional area for gas flow, which slightly increases the fluid velocity favoring mixing. In this work, we generalize the correlation by considering ceramic OCFs of different materials (zirconia, silicon carbon and alumina, with zirconia considered for the first time, to our knowledge) and pore density (30 and 45 ppi), with theoretical catalytic thicknesses ranging between 50 and 40 μm for the 30 and 45 ppi foams, respectively.

Fig. 9A/B shows the CH_4 conversion as a function of temperature for all coated OCFs (with 30 and 45 ppi) tested at different inlet CH_4 concentrations (0.5 and 1 vol%) and WHSV of 60 NL h^{-1} g_{cat}^{-1}. As observed, at 30 ppi, the Zir-OCF showed the best catalytic performance at both CH_4 concentrations compared to SiC and Alu OCFs, with almost no difference by varying the inlet methane concentration (Fig. 9A). The typical sigma-shape CH_4 conversion curves shifted at slightly higher temperature by increasing the pore density of the OCFs from 30 to 45 ppi, with a slight worsening of the performance with the increase of the inlet methane concentration (Fig. 9B). Similar and reproducible trends were recorded by testing the OCFs at WHSV of 30 and 90 NL h^{-1} g_{cat}^{-1}

Table 2
Correlations for the estimation of S_{ga} derived in literature for circular strut cross-sections.

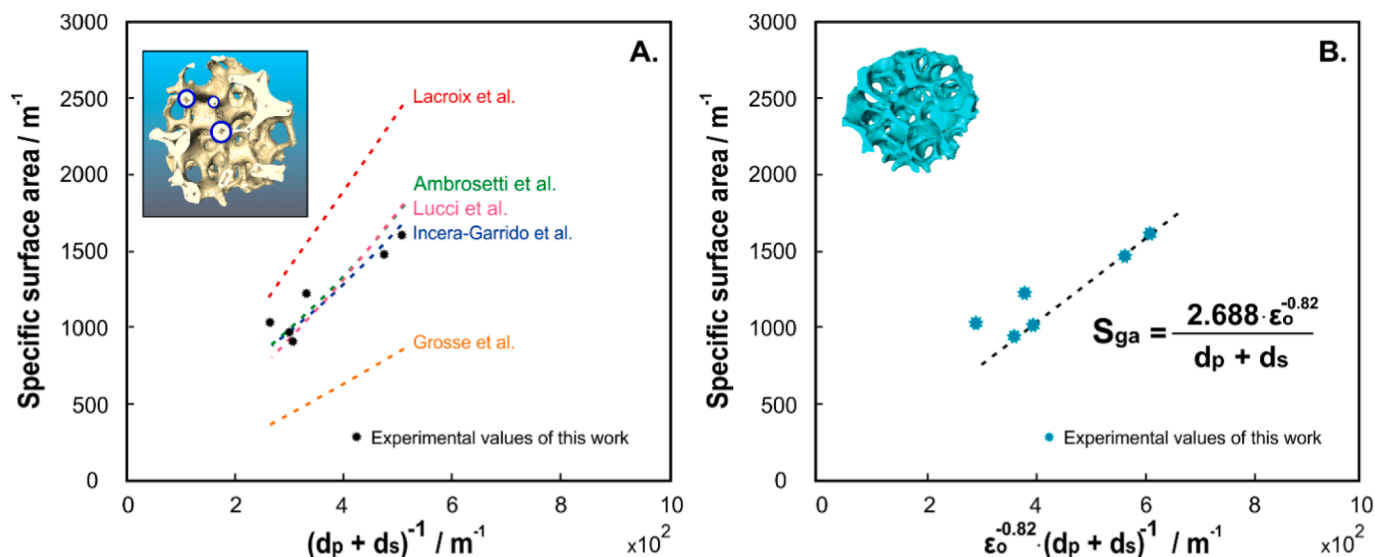| Reference	Cell model	S_{ga} [m^{-1}]
(Lacroix et al., 2007)	Cubic	$S_{ga} = \dfrac{4}{d_s} \cdot (1 - \varepsilon_o)$
(Incera Garrido et al., 2008)	Empirical	$S_{ga} = 3.84 \cdot \left(\dfrac{d_p + d_s}{m}\right)^{-0.85} \cdot \varepsilon_o^{-0.82}$
(Grosse et al., 2009)	Weaire-Phelan	$S_{ga} = \dfrac{4.84\sqrt{1 - \varepsilon_o} - 2.64 \bullet (1 - \varepsilon_o)}{d_p + d_s}$
(Lucci et al., 2014)	TKKD	$S_{ga} = \dfrac{10.33 \bullet \sqrt{1 - \varepsilon_o} - 5.8 \bullet (1 - \varepsilon_o)}{d_p + d_s}$
(Ambrosetti et al., 2017)	TKKD	$S_{ga} = \dfrac{-7.377 \bullet d_s^2 + 10.082 \bullet d_s \bullet d_c + 0.3548 \bullet d_c^2}{0.419 \bullet (d_c + d_s)^3}$

Fig. 8. (A) Trends of correlations reported in the literature for estimating the S_{ga} with an error ranging from 18 to 53%; (B) Correlation derived in this study to estimate the S_{ga} obtained from micro-CT measurements, with an average error below 12%.

(**Fig. S3**/**S4**/**S5** in the *Supplementary Information*), with differences more marked among the various sigma-shape CH_4 conversion curves at the highest WHSV and lowest ppi values. Overall, the best catalytic performance in all tested conditions belongs to the coated 30 ppi Zir OCF. While the Alu-OCF showed the lowest catalytic performance for all flow conditions studied.

In agreement with our previous studies, increasing the flow rate led to a shift of the CH_4 conversion curves towards higher temperatures for all coated OCFs. This shift can be attributed to the reduced contact time between the reactive gases and the catalyst surface, as clearly observed in Fig. 9.**C/D** (inlet CH_4 concentration 0.5 vol%, and Fig. S4**A/B** in the *Supporting Information* for inlet CH_4 concentration 1.0 vol%). These results can be analyzed by comparing the catalytic performance at equal pore density (Fig. 9**C/D** and Fig. S3**A/B**), and equal space velocity (Fig. 9**E/F** and Fig. S3**C/D**) Interestingly, we can observe the behavior of the T_{10} (corresponding to the reaction extinction, where the catalyst works in the kinetic regime) in the various operating conditions. Both 30 and 45 ppi Zir OCFs remain always the best performing systems in all tested conditions, but their corresponding T_{10} undergo a sharp worsening. While both 30 and 45 ppi SiC OCFs exhibit less variable values of the T_{10}. The difference of the T_{10} for the SiC OCFs, either at equal WHSV by increasing ppi, or at equal ppi but increasing WHSV ($\Delta T_{10 \ @ \ (90-30 \ WHSV)}$ or $\Delta T_{10 \ @ \ (45-30 \ ppi)}$) are smaller compared to the values of Alu and Zir OCFs. Table S3 in the *Supporting Information* highlights the delta temperatures. SiC OCFs favor the catalytic performance in the extinction zone and thus delay the reaction extinction. Even more, the SiC OCFs are rather insensible in terms of T_{10} to an increase of either the WHSV and inlet CH_4 concentration (the 45 ppi SiC OCF fed with 1.0 vol% operating at 90 WHSV exhibits a T_{10} lower than the corresponding T_{10} of the 30 ppi Zir OCF, Figure S3D).

The results shown in Fig. 9**E/F** and Fig. S3**C/D** can be explained by considering the difference of the volumetric heat transfer coefficients (Ercolino et al., 2017a, 2017c), which depend on the thermal conductivity values of the OCFs: they increase in the following order: Zir-OCF 2 · 10^4-0.5 · 10^5 W m^{-3} K^{-1} with $\lambda_{Zir} = 0.027$ W m^{-1} K^{-1} (Huo et al., 2016), Alu-OCF 1.5 · 10^5-9 · 10^5 W m^{-3} K^{-1} with $\lambda_{Alu} = 0.16$ W m^{-1} K^{-1} (Poco et al., 2001; Shimizu et al., 2013), SiC-OCF 2 · 10^5-1 · 10^6 W m^{-3} K^{-1} with $\lambda_{SiC} = 0.40$ W m^{-1} K^{-1}, (Fend et al., 2004). The thermal conductivity values of the OCFs are much lower, approximatively one order of magnitude, compared to the values of the corresponding bulk ceramic materials (zirconia, alumina and silicon carbide). The rather low values take into account the voidage of the foams due to their peculiar

configuration consisting of a dense solid skeleton, the strut, and air inglobated within (Scheffler and Colombo, 2005). More details on the thermal conductivity values can be found in the *Supporting Information*.

At low values of WHSV, the low thermal conductivity of Zir OCFs allows prevents the extinction of the reaction. While at high values of WHSV, Zir OCFs prevent extinction in a lesser extent, which occurs at higher temperatures. Instead, materials with higher thermal conductivity values such as SiC OCFs and, in a lesser extent Alu OCFs, favor the stabilization of the combustion reaction at higher values of WHSV, counterbalancing the more heat generated by the reaction and the reduction of the residence time. As a consequence, the extinction of the reaction is somehow delayed (and it occurs at temperatures similar to these of Zir OCFs). This is in agreement with our previous studies on external and internal heat transfer limitations of OCFs (Moncada Quintero et al., 2021a), where we observed that the heat removal for Zir-OCF is higher than the heat produced by the combustion reaction at bulk temperatures below 400 °C. Instead, for Alu and SiC OCFs is effects is noticeable at lower temperatures, below 300 °C. This means that at temperatures for which the heat generated by the reaction is higher than the heat removed, the performance of the process is in an unstable zone. This effect is appreciable for SiC and Alu OCFs where, especially at high WHSV, the sigma shape CH_4 conversion curves do not reach complete combustion. These findings are in agreement with the literature, in fact stability is strongly dependent on the thermal conductivity. It can be significantly improved using highly insulating materials at low inlet gas velocity, where extinction is likely to occur (Di Sarli, 2021; Kaisare and Di Sarli, 2021). Extinction is strongly affected by heat losses to the surrounding. Thus, at high space velocity, materials with high thermal conductivity are more suitable to stabilize the reaction by lowering the extinction (Chen et al., 2017; Kaisare and Vlachos, 2007). The same effect is appreciable when the pore density of the OCFs increases from 30 to 45: with more and smaller pores (Fig. 3), the superficial velocity increases and, consequently, mass and heat transfer are enhanced. Moreover, the thermal conductivity decreased with increasing cell density (Bianchi et al., 2013; Groppi and Tronconi, 2005; Visconti et al., 2013). Thus, for the more heat conductive OCFs, the conversion curves almost overlap and the extinction of the reaction occurs at temperatures very similar among them. We can conclude that the low thermal conductivity of Zir-OCF favor the exothermic combustion of CH_4, while the higher thermal conductivity of Alu- and SiC-OCFs favor the heat transfer necessary to maintain the catalytic activity of the reaction during the extinction. This effect is enhanced for high thermal conductivity OCFs
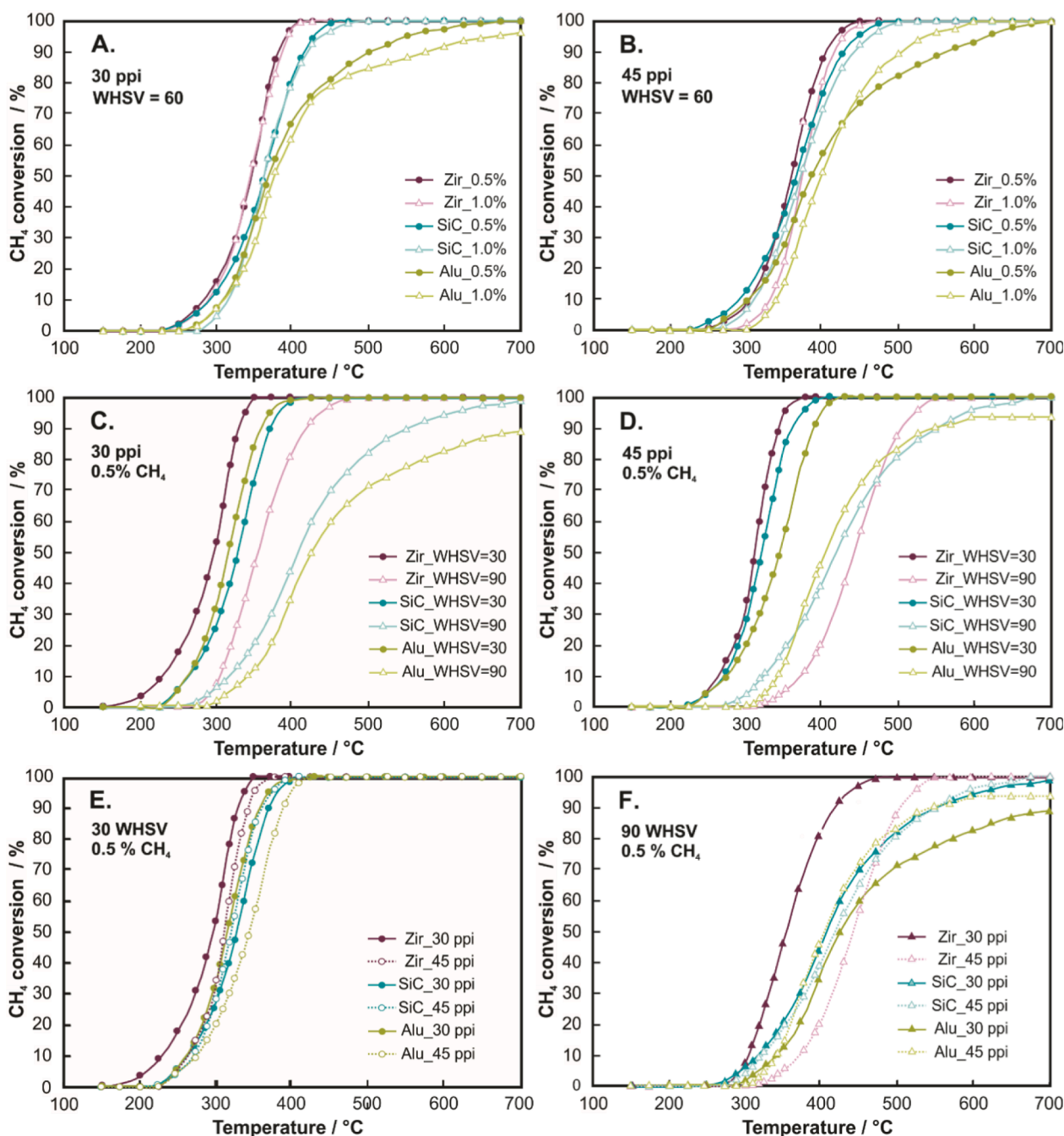
Fig. 9. CH$_4$ conversion versus temperature sigma-shape curves for all 30/45 ppi PdO/Co$_3$O$_4$ coated OCFs tested at different inlet CH$_4$ concentrations (0.5 and 1 vol %) and WHSV of 60 NL h^{-1} g$_{cat}^{-1}$ (A/B). Comparison of the various sigma-shape curves for all the OCFs tested at 0.5 vol% of inlet CH$_4$ concentration by keeping constant the porosity and varying the WHSV (C/D), or by keeping constant the WHSV and varying the porosity (E/F).

when the pore density increases.

The role of the thermal conductivity values on the combustion performance can be used on purpose to optimize the performance of catalytic reactor as a function of the operative condition. In fact, as reported in our previous work, by combining zirconia and silicon carbide foams of different lengths inside the reactor, the presence of the SiC foam in the gas inlet zone enabled to boost the ignition of the catalytic reaction at low temperature and to supply the heat required to maintain the reaction at lower shut-down temperature during the catalytic tests in the heating and cooling ramps, respectively. Recently, Kaisare and Di Sarli (Kaisare and Di Sarli, 2021) investigated the combined effect of catalyst placement and thermal conductivity on the stability of a micro-combustor using three configurations at different thermal

conductivity. The authors concluded that the extinction behavior was controlled by the catalytic reaction and that the lower conductivity walls provided significantly higher extinction resistance compared to the more conductive walls. Especially at low thermal conductivity, the catalytic inner wall plays a key role in determining the behavior at low fluid velocity, while at high thermal conductivity, the catalytic walls govern the behavior at high flow rate. Palma et al. (Palma et al., 2018) pointed out that the use of a structured catalyst with high thermal conductivity in exothermic reactions provides a better utilization of the entire catalytic volume by keeping the temperature almost constant in most of the catalyst, which leads to higher conversions, longer catalyst lifetime and avoids the formation of hot spots. Furthermore, they also stated that catalytic systems supported on open cell foams develop a

tortuous flow field that favors heat and mass transfer, generating a more homogeneous distribution of temperature and gas concentration, which allows to improve the performance of the catalytic process in comparison with monolithic structures.

Fig. 10 illustrates the operating regimes of catalytic OCFs at different temperatures as a function of the ratio between the characteristic mass transfer times and the reaction time, when feeding the reactor with a CH_4 concentration of 0.5 vol% and volumetric flow rate of 0.1 NL min^{-1} (WHSV = 30 NL h^{-1} g$_{cat}^{-1}$). At low temperatures (T less than 250 °C) the coated OCFs operate in a kinetic regime independently of the substrate pore density, showing CH_4 conversions of less than 10% (see Fig. 9C/D) and reaction times up to 6 orders of magnitude longer than the diffusion times. Expectedly, as the temperature increases, the reaction rate increases (according to the Arrhenius equation). Thus, the diffusional effects start to become important and the catalyst shifts from operating in a fully reaction-controlled regime to a transition or mixed regime (where the values of diffusive and kinetic resistances are comparable) or a regime governed by mass transfer. From the second Damköhler number (Da-II), it is known that diffusive effects occurring between the bulk gas and the catalyst surface begin to control the catalytic process when $Da_{II} > 0.1$, while that the governing of intraparticle mass transfer is indicated by the third Damköhler number when $Da_{III} > 1$. We report the expressions used to determine the Damköhler numbers in the *Supplementary Information* (**Equations S.1** and **S.2**). From Fig. 10.A, it can be seen that at 30 ppi, the catalytic structures operate in a transitional regime (or mixed regime) at temperatures between about 250 °C and 300 °C and above 700 °C. Conversely, at 45 ppi, the catalysts fall between a kinetic regime at temperatures below 250 °C and a mixed regime in which internal and external diffusional effects are comparable. According to Florén et al. (Florén et al., 2017), an operating region can be defined as limiting when its time scale is at least one order of magnitude larger with respect to the other characteristic times. In this way, at lower pore density, the SiC foam ranges between a kinetic regime at temperatures lower than ~ 260 °C and a mixed regime where the diffusion times are comparable but longer than the reaction time ($t_r < t_e \approx t_i$, **Equations S.3**, **S.4** and **S.5** in the *Supplementary Information*) at temperatures above 260 °C. Whereas for alumina and zirconia foams, the catalyst operates in a kinetic regime at temperatures below 235 °C, then, a further temperature increase allows moving from operating from a kinetic regime to a transitional regime (where the characteristic times of reaction and diffusion are similar) over the temperature range between 235–320 °C and 235–300 °C for alumina and zirconia, respectively. A subsequent increase in temperature leads to a further increase of the reaction rate, and thus of Da_{II}, governing the catalytic process external mass transfer at temperatures between 320–490 °C and

300–550 °C for alumina and zirconia, respectively. Finally, at temperatures higher than 490 °C for Alu-OCF and 550 °C for Zir-OCF, the catalyst returns to operate in a mixed regime. On the other hand, at 45 ppi, all three foams are banded between a kinetic regime at lower temperatures of about 300 °C and a mixed regime at higher temperatures (see Fig. 10B).

The mass transfer coefficients of the catalytic OCFs were estimated from CH_4 conversions under diffusion controlled conditions (asymptotic behavior of the extinction curve at medium/high temperatures). Under full control of external diffusion, the observed reaction rate is equal to the rate of transport of reactants through the gas phase in stationary conditions. Therefore, assuming that the reactor behaves as an isothermal plug flow with negligible axial dispersion, according to the CH_4 mass balance in steady-state conditions it follows that:

$$k_{m,OCF}^{e} = -\frac{\ln(1 - X_{CH_4})}{S_{ga} \cdot \left(\frac{V_f}{F^v}\right)} \tag{7}$$

where S_{ga} is the specific surface area, V_f is the volume of the catalytic foam, F^v is the total volumetric flow of the reactive gas mixture and X_{CH_4} is the methane conversion. Clearly, the increase in ppi leads to a decrease in foam pore diameter (as reported in Table S2), which reduces the cross-sectional area available for gas flow. Hence, at equal volumetric flow rate fed to the reactor and catalyst mass deposited on the foams, a higher ppi favors the mixing of the reactive gases thanks to the increase of the fluid velocity and thus of the mass transfer coefficients. This can be seen in the inspection of Fig. 11A/B, where regardless of the ceramic material nature, the smaller the pore diameter, the higher the mass transfer coefficient.

Mass transfer coefficients expressed in dimensionless form ($Sh = \frac{k_{m,OCF}^e \cdot d_p^c}{D_{CH_4,mix}}$) were plotted versus Reynolds number on a logarithmic scale in Fig. 11.B for all flow conditions investigated and then fitted by a single correlation of the form $Sh = A \cdot Re^m \cdot Sc^{\frac{1}{3}}$, obtaining:

$$Sh = 1.02 \cdot Re^{0.43} \cdot Sc^{1/3} \tag{8}$$

where Re is the Reynolds number (estimated assuming as characteristic length the coated pore diameter) and Sc is the Schmidt number (considering 1/3 as power value, according to the boundary layer theory). The diffusion coefficient of CH_4 in the gas mixture ($D_{CH_4,mix}$) at the system gas temperature was 3.24–17.18 × 10^{-5} m^2 s^{-1}. This correlation covers a range of open porosities (ε_o) from 0.78 to 0.86, pore diameters from 0.32 to 3.87 mm, pore density from 30 to 45 ppi, and a gamma of Re numbers varying from 2.2 to 9.5.

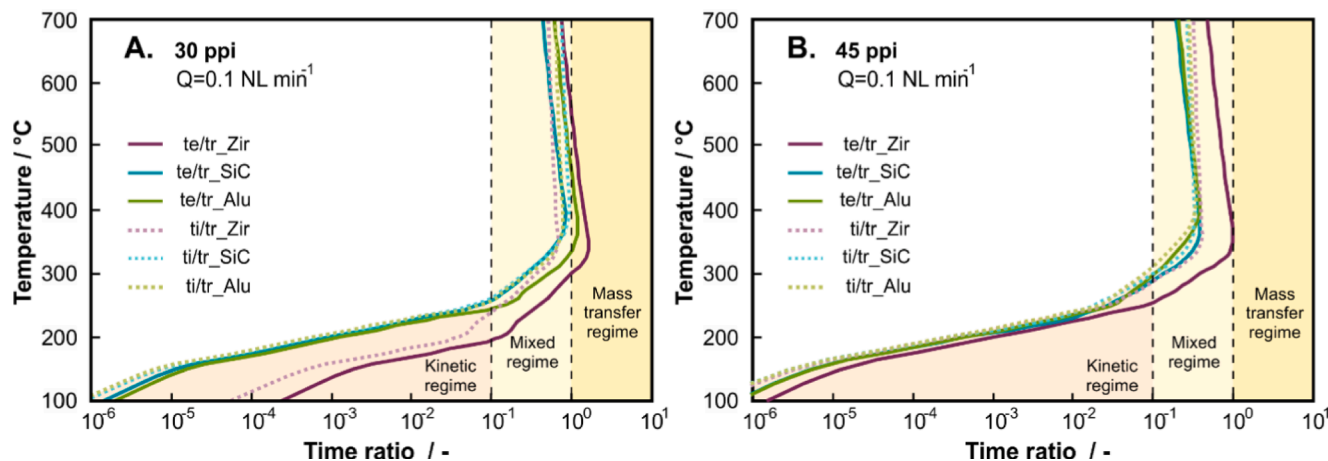Interestingly, Equation 6 closely resembles semi-theoretical corre-

Fig. 10. Operating regimes of catalytic OCFs at different temperatures as a function of the ratio between the characteristic mass transfer times and the reaction time, at 0.5 vol% of CH_4 and volumetric flow rate of 0.1 NL min^{-1} (WHSV = 30 NL h^{-1} g$_{cat}^{-1}$) for 30 (A) and 45 (B) ppi OCFs.
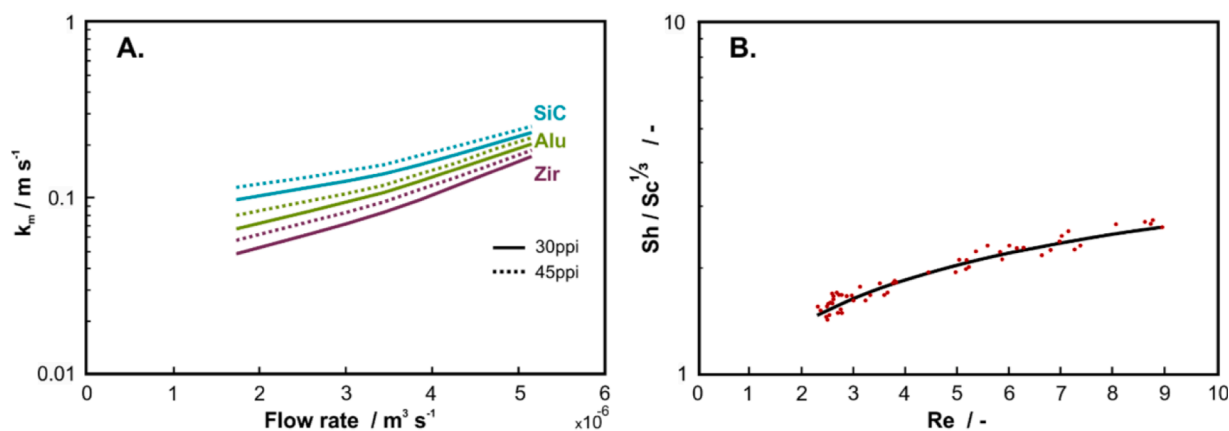
Fig. 11. Mass-transfer coefficients versus inlet flow rate estimated for different coated ceramic foams with 30 and 45 ppi at inlet CH_4 concentration of 0.5 vol% (A) and $Sh/Sc^{1/3}$ vs Re logarithmic plot, overall correlation of mass transfer data for all ceramic foams (B).

lations from literature that describe the heat transfer of flow through banks of pipes at low Reynolds number (Incropera et al., 2011). Furthermore, both the parameter *A* (which is a function of the porosity and geometric properties of the foam) and the exponent *m* (that characterizes the dependence of the Sherwood number with the magnitude of the velocity) are consistent with the values reported in several studies of OCFs made of different materials (ceramic and metallic) and pore densities (10–45 ppi) (Aguirre et al., 2020; Giani et al., 2005; Groppi et al., 2007; Incera Garrido et al., 2008; Schlegel et al., 1993). Schlegel et al. (Schlegel et al., 1993) measured convective heat transfer coefficients in cordierite ceramic OCFs with pore densities of 10, 20, 30 and 50 ppi and open porosities between 0.84 and 0.87. The heat transfer measurements performed by the authors were carried out with negligible radiation, hence the Colburn analogy (Chilton and Colburn, 1934) can be used for comparison. The *Nu* values of these authors are in good agreement with the experimental *Sh* numbers estimated in this work at pore densities of 30 ppi. Incera Garrido et al. (Incera Garrido et al., 2008) also measured mass transfer coefficients in alumina foams of different ppi (10, 20, 30 and 45 pore per inch) and ε_o (0.80 and 0.85), while CO conversion was monitored during oxidation in Pt/SnO_2 coated OCFs under external mass transfer control. The authors showed a systematic variation of the parameters characterizing the correlation with foam pore size and porosity. On the other hand, Groppi et al. (Giani et al., 2005; Groppi et al., 2007) proposed a generalized correlation for mass transfer in metallic and ceramic foams based on a simple cubic cell description of the complex foam structure. The expression was derived from CO combustion tests performed under gas/solid diffusional control on FeCrAlloy foams with high void fractions ($\varepsilon_o > 0.90$) and pore densities in the range of 5–15 ppi. They found that the geometric *A* value of the correlation fitting both materials was 0.91, while the dependence of Sherwood number on Reynold number was 0.43. These values are in agreement with those obtained in this study despite the difference in the geometrical properties of the foams. On this regard, taking into account the literature results and those obtained in this work, it is clear that the decrease of the pore density improves the mixing, owing to the higher intensity of the turbulence expected for the external flow inside the smaller pores.

3.5. Pressure drop measurements

Fig. 12**A** shows the measured pressure drop values for all OCFs by varying the N_2 flow rate in the reactor. As observed, for all foam materials, the increase in nominal pore density leads to a higher pressure drop. This can be explained by the variation in the surface area to volume ratio of the samples, since the higher the ppi, the smaller the pore diameter and the larger the specific surface area, resulting in higher fluid

resistance. In particular, Zir foams exhibited slightly lower pressure drops compared to SiC and Alu foams at the same ppi. This is in line with the values obtained for S_{ga}, $\varepsilon_{o,m}$, and d_p for each foam material at the same pore density. The Forchheimer-extended Darcy model (Bhatta-charya et al., 2002; Boomsma et al., 2003; Hamadouche et al., 2016) (Equation 1) is a good fit to our experimental data. By adjusting the pressure drop values of the foams as a quadratic function of the fluid velocity, it was also possible to determine the viscous and inertial constants (*a* and *b* of Equation 1) and thus estimate the respective permeability values, as listed in Table 3. Clearly, an increase in pore density from 30 to 45 ppi leads to a decrease in k_1 and k_2 values. As mentioned in the previous sections, an increase in pore density means a larger number of pores enclosed in the same space, with a consequent reduction in cell volume and an increment in the number of struts (solid phase). This results in an increase in viscous effects on the pressure drop, owing to a reduction of the area available for flow passage which affects k_1, and an increase in the tortuosity of the medium which intensifies the inertial effects and reduces k_2 (Innocentini et al., 1999, 1998).

In the literature, alumina foam has been extensively studied at different ppi and ε_o (Dietrich et al., 2009; Incera Garrido et al., 2008; Italiano et al., 2018; Lacroix et al., 2007; Moreira et al., 2004; Richardson et al., 2000). Moreover, silicon carbide foams have been mostly studied in the literature in their combined form, such as sintered silicon carbide (SSiC (Inayat et al., 2016)), oxide bonded silicon carbide (OBSiC (Dietrich et al., 2009)), 50 wt% $SiC-Al_2O_3$ mixture (Innocentini et al., 1999) and infiltrated silicon carbide (SiSiC (Hernandez Camacho et al., 2019; Zalucky et al., 2015)). No data on zirconium foams have been found in the literature, hence only the data obtained in this work are listed. Fig. 12**B** compares the results of the pressure drop values as a function of gas velocity in ceramic OCFs of different pore density and porosity reported in the literature with the ones obtained in this work. The deviations obtained in terms of pressure drop (Fig. 12**B**) can be attributed to different factors. One of the possible reasons is the discrepancy in pore diameter for the same number of pores per inch, in foams fabricated by different manufacturers. Since they do not represent a standard measurement, these values may vary from one manufacturer to another, directly affecting the foam geometry. Furthermore, the amount of closed pores in the foam sample can vary substantially, leading to significant deviations in pressure drop between authors. On the other hand, the order of magnitude of the viscous and inertial permeability values (10^{-9}-10^{-8} m^2 for k_1 and 10^{-3} m for k_2, where both permeabilities decrease in the order of Zir > Alu > SiC) is in agreement with the data reported in the literature (see Table S4).
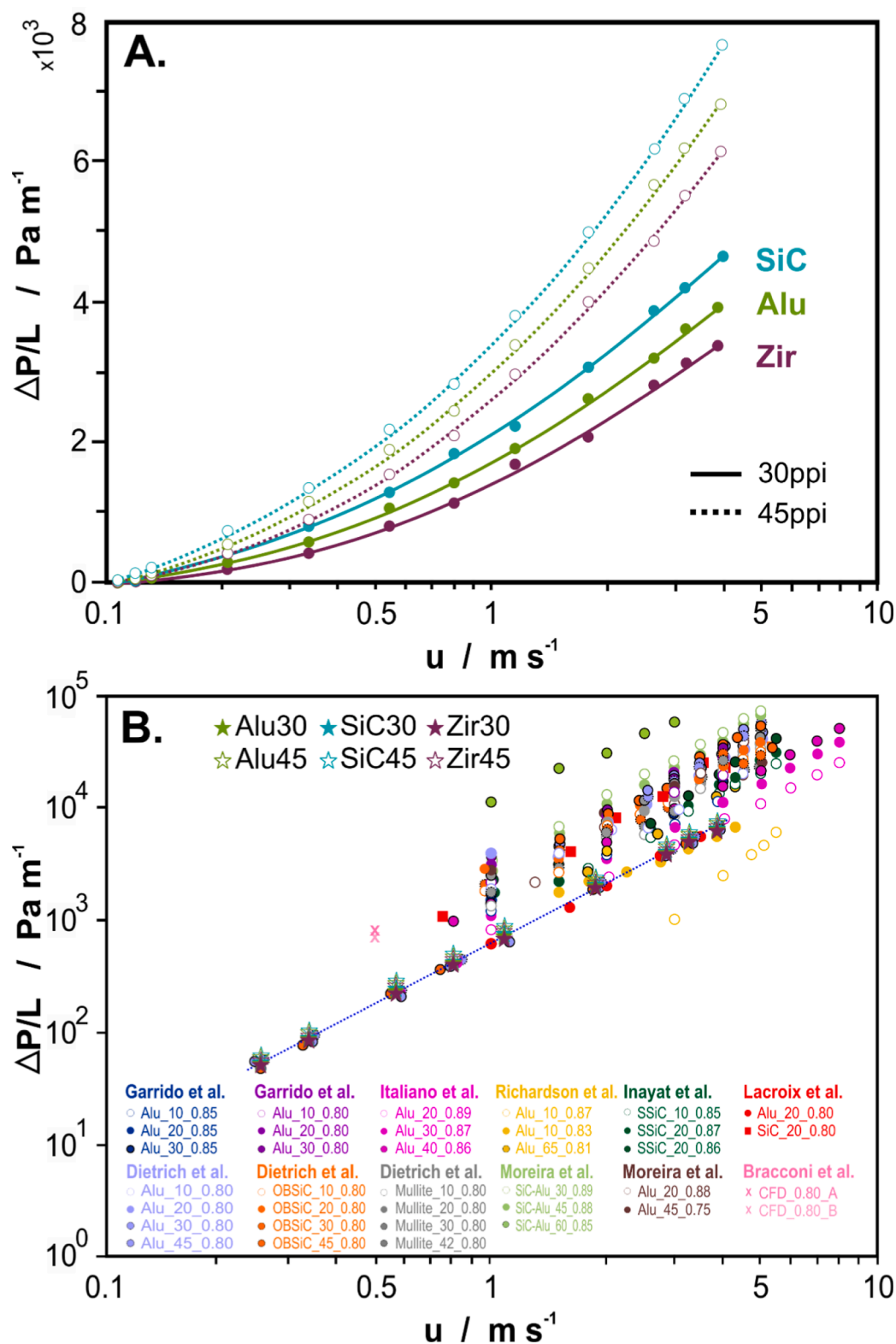
Fig. 12. Pressure drop measurements across Alu, SiC, and Zir OCFs (30 and 45 ppi) as a function of the superficial velocity: experimental data and curves derived by the Forchheimer-extended Darcy model (Bhattacharya et al., 2002; Boomsma et al., 2003; Hamadouche et al., 2016) and measurements performed in N_2 flow at ambient temperature (A). Pressure drop values as a function of superficial velocity for various ceramic OCFs collected from the literature and compared with the values obtained in this work (B).

4. Conclusions

Ceramic open cell foams made of zirconia, silicon carbide and alumina with nominal pore densities of 30 and 45 ppi have been characterized using the micro-CT technique. Characteristic dimensions such as pore size, strut diameter, and strut length as well as open porosity and specific surface geometry have been experimentally measured. For all ceramic structures the increase in nominal pore density led to a much more compact structure due to the higher number of cells and hence of strut per unit volume. The zirconia foam showed larger dimensions in terms of pore diameter, strut length and strut diameter at both nominal ppi values studied. The estimated experimental pore density was not congruent with the manufacturer's definition of pores per linear inch. Dense grains and microporous walls caused by the replication technique

Table 3
Viscous and inertial permeability values for the analyzed foams.

ppi	Alu		SiC		Zir	
	30	45	30	45	30	45
k_1 (m^2)	1.02E-08	5.75E-09	8.23E-09	5.06E-09	1.25E-08	6.54E-09
k_2 (m)	6.08E-03	3.12E-03	4.39E-03	2.73E-03	7.81E-03	3.59E-03

applied by the manufacturer were evidenced in all foam skeletons. Furthermore, all foams showed circular strut cross sections at open porosities below 85 %. On the other hand, the specific surface area of the foams increased with increasing pore density, where theoretical models based on the Kelvin cell provided a much closer approximation to the experimental values obtained. An empirical correlation that allows to determine the specific surface area of ceramic foams at porosities in the range 78–86 % was proposed. From the catalytic tests it was found that on average the best catalytic performance belongs to zirconia OCFs. In any case, when the catalyst operated in a kinetic regime (at low temperatures), SiC OCFs showed better catalytic activity, exhibiting almost same or lower extinction temperatures than those of Alu and Zir OCFs, when operated at high weight hourly space velocity, high inlet CH_4 concentrations. In fact, the stability of the reaction can be guaranteed with low thermal conductivity materials at low inlet gas velocity, where reaction extinction can easily occur, and with high thermal conductivity materials when the inlet gas velocity increases. The proposed mass transfer correlation for open cell ceramic foams resembles those reported in the literature. Finally, a series of measurements of the pressure drop across our OCFs pointed out that our foams follow the Forchheimer-extended Darcy model. The results obtained in this work provide an opportunity for detailed modeling and fluid dynamic studies based on open cell foams.

Funding sources

CRediT authorship contribution statement

Carmen W. Moncada Quintero: Conceptualization, Methodology, Investigation, Data curation, Formal analysis, Validation, Writing – original draft, Writing – review & editing. **Hernan G. Mazzei:** Investigation, Data curation, Formal analysis. **Marion Servel:** Data curation, Validation. **Frédéric Augier:** Methodology, Formal analysis, Validation. **Yacine Haroun:** Investigation, Data curation, Formal analysis, Validation, Writing – original draft. **Jean-François Joly:** Conceptualization, Supervision, Writing – review & editing, Resources. **Stefania Specchia:** Conceptualization, Methodology, Validation, Supervision, Writing – review & editing, Funding acquisition, Resources.

Declaration of Competing Interest

The authors declare that they have no known competing financial interests or personal relationships that could have appeared to influence the work reported in this paper.

Data availability

Data will be made available on request.

Acknowledgements

Appendix A. Supplementary data

Supplementary data to this article can be found online at https://doi.org/10.1016/j.ces.2023.119138.

References

Aguirre, A., Chandra, V., Peters, E.A.J.F., Kuipers, J.A.M., Neira D'Angelo, M.F., 2020. Open-cell foams as catalysts support: A systematic analysis of the mass transfer limitations. Chem. Eng. J. 393, 124656 https://doi.org/10.1016/j.cej.2020.124656.

Ahmad, R., Ha, J.-H., Song, I.-H., 2014. Processing Methods for the Preparation of Porous Ceramics. J. Korean Powder Metall. Inst. 21, 389–398. https://doi.org/10.4150/kpmi.2014.21.5.389.

Ambrosetti, M., Bracconi, M., Groppi, G., Tronconi, E., 2017. Analytical Geometrical Model of Open Cell Foams with Detailed Description of Strut-Node Intersection. Chem.-Ing.-Tech. 89, 915–925. https://doi.org/10.1002/cite.201600173.

Ashraf, M.A., Sanz, O., Italiano, C., Vita, A., Montes, M., Specchia, S., 2018. Analysis of Ru/La-Al2O3 catalyst loading on alumina monoliths and controlling regimes in methane steam reforming. Chem. Eng. J. 334, 1792–1807. https://doi.org/10.1016/j.cej.2017.11.154.

Balzarotti, R., Ambrosetti, M., Beretta, A., Groppi, G., Tronconi, E., 2020. Investigation of packed conductive foams as a novel reactor configuration for methane steam reforming. Chem. Eng. J. 391, 123494 https://doi.org/10.1016/j.cej.2019.123494.

Banhart, J., 2001. Manufacture, characterisation and application of cellular metals and metal foams. Prog. Mater. Sci. 46, 559–632. https://doi.org/10.1016/S0079-6425(00)00002-5.

Banhart, J., Weaire, D., 2011. On the Road Again: Metal Foams Find Favor 37–42. https://doi.org/10.1063/1.1506749.

Baroutaji, A., Carton, J.G., Stokes, J., Olabi, A.G., 2017. Application of Open Pore Cellular Foam for air breathing PEM fuel cell. Int. J. Hydrogen Energy 42, 25630–25638. https://doi.org/10.1016/j.ijhydene.2017.05.114.

Béchet, E., Cuilliere, J.C., Trochu, F., 2002. Generation of a finite element MESH from stereolithography (STL) files. CAD Comput. Aided Des. 34, 1–17. https://doi.org/10.1016/S0010-4485(00)00146-9.

Bernard, P., Stelmachowski, P., Broś, P., Makowski, W., Kotarba, A., 2021. Demonstration of the Influence of Specific Surface Area on Reaction Rate in Heterogeneous Catalysis. J. Chem. Educ. 98, 935–940. https://doi.org/10.1021/acs.jchemed.0c01101.

Bhattacharya, A., Calmidi, V.V., Mahajan, R.L., 2002. Thermophysical properties of high porosity metal foams. Int. J. Heat Mass Transf. 45, 1017–1031. https://doi.org/10.1016/S0017-9310(01)00220-4.

Bianchi, E., Heidig, T., Visconti, C.G., Groppi, G., Freund, H., Tronconi, E., 2013. Heat transfer properties of metal foam supports for structured catalysts: Wall heat transfer coefficient. Catal. Today 216, 121–134. https://doi.org/10.1016/j.cattod.2013.06.019.

Boomsma, K., Poulikakos, D., Ventikos, Y., 2003. Simulations of flow through open cell metal foams using an idealized periodic cell structure. Int. J. Heat Fluid Flow 24, 825–834. https://doi.org/10.1016/j.ijheatfluidflow.2003.08.002.

Bracconi, M., Ambrosetti, M., Maestri, M., Groppi, G., Tronconi, E., 2017. A systematic procedure for the virtual reconstruction of open-cell foams. Chem. Eng. J. 315, 608–620. https://doi.org/10.1016/j.cej.2017.01.069.

Bracconi, M., Ambrosetti, M., Okafor, O., Sans, V., Zhang, X., Ou, X., Da Fonte, C.P., Fan, X., Maestri, M., Groppi, G., Tronconi, E., 2019. Investigation of pressure drop in 3D replicated open-cell foams: Coupling CFD with experimental data on additively manufactured foams. Chem. Eng. J. 377, 120123 https://doi.org/10.1016/j.cej.2018.10.060.

Bracconi, M., Ambrosetti, M., Maestri, M., Groppi, G., Tronconi, E., 2020. Analysis of the effective thermal conductivity of isotropic and anisotropic Periodic Open Cellular Structures for the intensification of catalytic processes. Chem. Eng. Process. - Process Intensif. 158, 108169 https://doi.org/10.1016/j.cep.2020.108169.

Buciuman, F.C., Kraushaar-Czarnetzki, B., 2003. Ceramic Foam Monoliths as Catalyst Carriers. 1. Adjustment and Description of the Morphology. Ind. Eng. Chem. Res. 42, 1863–1869. https://doi.org/10.1021/ie0204134.

Calmidi, V.V., Mahajan, R.L., 1999. The effective thermal conductivity of high porosity fibrous metal foams. J. Heat Transfer 121, 466–471. https://doi.org/10.1115/1.2826001.

Chen, J., Song, W., Xu, D., 2017. Optimal combustor dimensions for the catalytic combustion of methane-air mixtures in micro-channels. Energy Convers. Manag. 134, 197–207. https://doi.org/10.1016/j.enconman.2016.12.028.

Chilton, T.H., Colburn, A.P., 1934. Mass transfer (absorption) coefficients — production from data on heat transfer and fluid friction. Ind. Eng. Chem. 26 (1934), 1183. https://doi.org/10.1021/ie50299a012.

Ciambelli, P., Palma, V., Palo, E., 2010. Comparison of ceramic honeycomb monolith and foam as Ni catalyst carrier for methane autothermal reforming. Catal. Today 155, 92–100. https://doi.org/10.1016/j.cattod.2009.01.021.

Cristiani, C., Finocchio, E., Latorrata, S., Visconti, C.G., Bianchi, E., Tronconi, E., Groppi, G., Pollesel, P., 2012. Activation of metallic open-cell foams via washcoat deposition of Ni/MgAl 2O 4 catalysts for steam reforming reaction. Catal. Today 197, 256–264. https://doi.org/10.1016/j.cattod.2012.09.003.

Della Torre, A., Lucci, F., Montenegro, G., Onorati, A., Dimopoulos Eggenschwiler, P., Tronconi, E., Groppi, G., 2016. CFD modeling of catalytic reactions in open-cell foam substrates. Comput. Chem. Eng. 92, 55–63. https://doi.org/10.1016/j.compchemeng.2016.04.031.

Di Sarli, V., 2021. The effect of differentiating the thermal conductivity between inner and outer walls on the stability of a u-bend catalytic heat-recirculating micro-combustor: A cfd study. Appl. Sci. 11 https://doi.org/10.3390/app11125418.

Dietrich, B., Schabel, W., Kind, M., Martin, H., 2009. Pressure drop measurements of ceramic sponges-determining the hydraulic diameter. Chem. Eng. Sci. 64, 3633–3640. https://doi.org/10.1016/j.ces.2009.05.005.

Ercolino, G., Karimi, S., Stelmachowski, P., Specchia, S., 2017a. Catalytic combustion of residual methane on alumina monoliths and open cell foams coated with Pd/Co3O4. Chem. Eng. J. 326, 339–349. https://doi.org/10.1016/j.cej.2017.05.149.

Ercolino, G., Stelmachowski, P., Grzybek, G., Kotarba, A., Specchia, S., 2017b. Optimization of Pd catalysts supported on Co3O4 for low-temperature lean combustion of residual methane. Appl. Catal. B Environ. 206, 712–725. https://doi.org/10.1016/j.apcatb.2017.01.055.

Ercolino, G., Stelmachowski, P., Specchia, S., 2017c. Catalytic performance of Pd/Co3O4 on SiC and ZrO2 open cell foams for process intensification of methane combustion in lean conditions. Ind. Eng. Chem. Res. 56, 6625–6636. https://doi.org/10.1021/acs.iecr.7b01087.

Favata, A., 2012. On the Kelvin problem. J. Elast. 109, 189–204. https://doi.org/10.1007/s10659-012-9375-4.

Fend, T., Hoffschmidt, B., Pitz-Paal, R., Reutter, O., Rietbrock, P., 2004. Porous materials as open volumetric solar receivers: experimental determination of thermophysical and heat transfer properties. Energy 29, 823–833. https://doi.org/10.1016/S0360-5442(03)00188-9.

Florén, C.-R., Maxime, V. den B., Derek, C., Henrik, G., Per-Anders, C., Heikki, K., Magnus, S., 2017. Modelling complete methane oxidation over palladium oxide in a porous catalyst using first-principles sur- face kinetics. Catal. Sci. Technol. 1–13. https://doi.org/10.1039/C7CY02135F.

Gao, H.B., Qu, Z.G., Feng, X.B., Tao, W.Q., 2012. Methane/air premixed combustion in a two-layer porous burner with different foam materials. Fuel 115, 154–161. https://doi.org/10.1016/j.fuel.2013.06.023.

García-Moreno, F., 2016. Commercial applications of metal foams: Their properties and production. Materials (Basel). 9, 20–24. https://doi.org/10.3390/ma9020085.

Ghazi, A., Berke, P., Tiago, C., Massart, T.J., 2020. Computed tomography based modelling of the behaviour of closed cell metallic foams using a shell approximation. Mater. Des. 194, 108866 https://doi.org/10.1016/j.matdes.2020.108866.

Giani, L., Groppi, G., Tronconi, E., 2005. Mass-transfer characterization of metallic foams as supports for structured catalysts. Ind. Eng. Chem. Res. 44, 4993–5002. https://doi.org/10.1021/ie0490886.

Gibson, L.J., Ashby, M.F., 1988. Cellular solids: Structure and Properties. J. Biomech. https://doi.org/10.1016/0021-9290(89)90056-0.

Groppi, G., Giani, L., Tronconi, E., 2007. Generalized correlation for gas/solid mass-transfer coefficients in metallic and ceramic foams. Ind. Eng. Chem. Res. 46, 3955–3958. https://doi.org/10.1021/ie061330g.

Groppi, G., Tronconi, E., 2005. Honeycomb supports with high thermal conductivity for gas/solid chemical processes. Catal. Today 105, 297–304. https://doi.org/10.1016/j.cattod.2005.06.041.

Große, J., Dietrich, B., Martin, H., Kind, M., Vicente, J., Hardy, E.H., 2008. Volume image analysis of ceramic sponges. Chem. Eng. Technol. 31, 307–314. https://doi.org/10.1002/ceat.200700403.

Grosse, J., Dietrich, B., Garrido, G.I., Habisreuther, P., Zarzalis, N., Martin, H., Kind, M., Bettina, K.C., 2009. Morphological characterization of ceramic sponges for applications in chemical engineering. Ind. Eng. Chem. Res. 48, 10395–10401. https://doi.org/10.1021/ie900651c.

Haack, D.P., Butcher, K.R., Kim, T., Lu, T.J., 2001. Novel Lightweight Metal Foam Heat Exchangers. Am Soc. Mech. Eng. Process Ind. Div. PID 6, 141–147.

Habisreuther, P., Djordjevic, N., Zarzalis, N., 2009. Statistical distribution of residence time and tortuosity of flow through open-cell foams. Chem. Eng. Sci. 64, 4943–4954. https://doi.org/10.1016/j.ces.2009.07.033.

Hamadouche, A., Nebbali, R., Benahmed, H., Kouidri, A., Bousri, A., 2016. Experimental investigation of convective heat transfer in an open-cell aluminum foams. Exp. Therm. Fluid Sci. 71, 86–94. https://doi.org/10.1016/j.expthermflusci.2015.10.009.

Hernandez Camacho, J.N., Lecrivain, G., Schubert, M., Hampel, U., 2019. Droplet retention time and pressure drop in sisic open-cell foams used as droplet separation devices: a numerical approach. Ind. Eng. Chem. Res. https://doi.org/10.1021/acs.iecr.9b04247.

Ho, P.H., De Nolf, W., Ospitali, F., Beton, D., Torkuhl, L., Fornasari, G., Vaccari, A., Benito, P., 2019. Insights into coated NiCrAl open-cell foams for the catalytic partial oxidation of CH4. React. Chem. Eng. 4, 1768–1778. https://doi.org/10.1039/c9re00178f.

Huo, W.-L., Zhang, X.-Y., Chen, Y.-G., Lu, Y.-J., Liu, W.-T., Xi, X.-Q., Wang, Y.-L., Xu, J., Yang, J.-L., 2016. Highly porous zirconia ceramic foams with low thermal conductivity from particle-stabilized foams. J. Am. Ceram. Soc. 99, 3512–3515. https://doi.org/10.1111/jace.14555.

Huu, T.T., Lacroix, M., Pham Huu, C., Schweich, D., Edouard, D., 2009. Towards a more realistic modeling of solid foam: use of the pentagonal dodecahedron geometry. Chem. Eng. Sci. 64, 5131–5142. https://doi.org/10.1016/j.ces.2009.08.028.

Inayat, A., Freund, H., Zeiser, T., Schwieger, W., 2011. Determining the specific surface area of ceramic foams: the tetrakaidecahedra model revisited. Chem. Eng. Sci. 66, 1179–1188. https://doi.org/10.1016/j.ces.2010.12.031.

Inayat, A., Klumpp, M., Lämmermann, M., Freund, H., Schwieger, W., 2016. Development of a new pressure drop correlation for open-cell foams based completely on theoretical grounds: taking into account strut shape and geometric tortuosity. Chem. Eng. J. 287, 704–719. https://doi.org/10.1016/j.cej.2015.11.050.

Incera Garrido, G., Patcas, F.C., Lang, S., Kraushaar-Czarnetzki, B., 2008. Mass transfer and pressure drop in ceramic foams: A description for different pore sizes and porosities. Chem. Eng. Sci. 63, 5202–5217. https://doi.org/10.1016/j.ces.2008.06.015.

Incropera, F.P., DeWitt, D.P., Bergman, T.L., Lavine, A.S., 2011. Fundamentals of Heat and Mass Transfer.

Innocentini, M.D.M., Sepulveda, P., Salvini, V.R., Pandolfelli, V.C., Coury, J.R., 1998. Permeability and structure of cellular ceramics: a comparison between two preparation techniques. J. Am. Ceram. Soc. 81, 3349–3352. https://doi.org/10.1111/j.1151-2916.1998.tb02782.x.

Innocentini, M.D.M., Salvini, V.R., Macedo, A., Pandolfelli, V.C., 1999. Prediction of ceramic foams permeability using Ergun's equation. Mater. Res. 2, 283–289. https://doi.org/10.1590/s1516-14391999000400008.

Italiano, C., Ashraf, M.A., Pino, L., Moncada Quintero, C.W., Specchia, S., Vita, A., 2018. Rh/CeO2 thin catalytic layer deposition on alumina foams: catalytic performance and controlling regimes in biogas reforming processes. Catalysts 8, 1–25. https://doi.org/10.3390/catal8100448.

Kaisare, N.S., Di Sarli, V., 2021. The effect of catalyst placement on the stability of a u-bend catalytic heat-recirculating micro-combustor: a numerical investigation. Catalysts 11. https://doi.org/10.3390/catal11121560.

Kaisare, N.S., Vlachos, D.G., 2007. Optimal reactor dimensions for homogeneous combustion in small channels. Catal. Today 120, 96–106. https://doi.org/10.1016/j.cattod.2006.07.036.

Kim, T.B., Yue, S., Zhang, Z., Jones, E., Jones, J.R., Lee, P.D., 2014. Additive manufactured porous titanium structures: through-process quantification of pore and strut networks. J. Mater. Process. Technol. 214, 2706–2715. https://doi.org/10.1016/j.jmatprotec.2014.05.006.

Kraynik, A.M., Reinelt, D.A., van Swol, F., 2003. Structure of random monodisperse foam. Phys. Rev. E 67, 031403. https://doi.org/10.1103/PhysRevE.67.031403.

Kuhlmann, K., Sinn, C., Siebert, J.M.U., Wehinger, G., Thöming, J., Pesch, G.R., 2022. From μCT data to CFD: an open-source workflow for engineering applications. Eng. Appl. Comput. Fluid Mech. 16, 1706–1723. https://doi.org/10.1080/19942060.2022.2109758.

Kumar, P., 2015. Investigation of Kelvin-like solid foams for potential engineering applications: an attractive set of geometrical and thermo-hydraulic properties. Aix-Marseille University.

Kumar, P., Topin, F., Tadrist, L., 2015. Geometrical characterization of Kelvin-like metal foams for different strut shapes and porosity. J. Porous Media 18, 637–652. https://doi.org/10.1615/JPorMedia.v18.i6.70.

Lacroix, M., Nguyen, P., Schweich, D., Pham Huu, C., Savin-Poncet, S., Edouard, D., 2007. Pressure drop measurements and modeling on SiC foams. Chem. Eng. Sci. 62, 3259–3267. https://doi.org/10.1016/j.ces.2007.03.027.

Lanik Foam Ceramics [WWW Document], n.d. URL https://www.lanik.eu/en/ (accessed 2.21.21).

Liang, X., Li, Y., He, Z., Wang, Q., Chen, Y., Xu, X., Li, B., Aneziris, C.G., 2019. Design of three-layered struts in SiC reticulated porous ceramics for porous burner. Ceram. Int. 45, 8571–8576. https://doi.org/10.1016/j.ceramint.2019.01.175.

Lindblad, J., 2005. Surface area estimation of digitized 3D objects using weighted local configurations. Image Vis. Comput. 23, 111–122. https://doi.org/10.1016/j.imavis.2004.06.012.

Lorensen, W.E., Cline, H.E., 1987. Marching cubes: a high resolution 3D surface construction algorithm. Comput. Graph. 21, 163–169. https://doi.org/10.1145/37402.37422.

Lu, T.J., Stone, H.A., Ashby, M.F., 1998. Heat transfer in open-cell metal foams. Acta Mater. 46, 3619–3635. https://doi.org/10.1016/S1359-6454(98)00031-7.

Lucci, F., Della Torre, A., von Rickenbach, J., Montenegro, G., Poulikakos, D., Dimopoulos Eggenschwiler, P., 2014. Performance of randomized Kelvin cell structures as catalytic substrates: mass-transfer based analysis. Chem. Eng. Sci. 112, 143–151. https://doi.org/10.1016/j.ces.2014.03.023.

G. Maliaris N. Michailidis Modeling of open cell structures geometry and mechanical response applying the Voronoi tessellation algorithm K.-.-D. Bouzakis EEAM and PCCM 2014 Thessaloniki 393 402 https://doi.org/10.13140/2.1.2342.3689.

Mancin, S., Zilio, C., Cavallini, A., Rossetto, L., 2010. Heat transfer during air flow in aluminum foams. Int. J. Heat Mass Transf. 53, 4976–4984. https://doi.org/10.1016/j.ijheatmasstransfer.2010.05.033.

Mancin, S., Zilio, C., Diani, A., Rossetto, L., 2013. Air forced convection through metal foams: experimental results and modeling. Int. J. Heat Mass Transf. 62, 112–123. https://doi.org/10.1016/j.ijheatmasstransfer.2013.02.050.

Mao, X., 2018. Processing of Ceramic Foams, in: Uday M. Basheer Al-Naib (Ed.), Recent Advances in Porous Ceramics. IntechOpen Limited, London. https://doi.org/10.5772/intechopen.71006.

Mirdrikvand, M., Sadeghi, M., Karim, M.N., Thöming, J., Dreher, W., 2020. Pore-scale analysis of axial and radial dispersion coefficients of gas flow in macroporous foam monoliths using NMR-based displacement measurements. Chem. Eng. J. 388, 124234 https://doi.org/10.1016/j.cej.2020.124234.

Moncada Quintero, C.W., Ercolino, G., Poozhikunnath, A., Maric, R., Specchia, S., 2021a. Analysis of heat and mass transfer limitations for the combustion of methane emissions on PdO/Co3O4 coated on ceramic open cell foams. Chem. Eng. J. 405, 126970 https://doi.org/10.1016/j.cej.2020.126970.

Moncada Quintero, C.W., Ercolino, G., Specchia, S., 2021b. Effect of the Co3O4 load on the performance of PdO/Co3O4/ZrO2 open cell foam catalysts for the lean combustion of methane: kinetic and mass transfer regimes. Catal. Today. https://doi.org/10.1016/j.cattod.2021.03.014.

Moncada Quintero, C.W., Ercolino, G., Specchia, S., 2022. Combined silicon carbide and zirconia open cell foams for the process intensification of catalytic methane combustion in lean conditions: impact on heat and mass transfer. Chem. Eng. J. 429, 132448 https://doi.org/10.1016/j.cej.2021.132448.

Montminy, M.D., Tannenbaum, A.R., MacOsko, C.W., 2004. The 3D structure of real polymer foams. J. Colloid Interface Sci. 280, 202–211. https://doi.org/10.1016/j.jcis.2004.07.032.

Moreira, E.A., Innocentini, M.D.M., Coury, J.R., 2004. Permeability of ceramic foams to compressible and incompressible flow. J. Eur. Ceram. Soc. 24, 3209–3218. https://doi.org/10.1016/j.jeurceramsoc.2003.11.014.

Neethirajan, S., Karunakaran, C., Jayas, D.S., White, N.D.G., 2006. X-ray computed tomography image analysis to explain the airflow resistance differences in grain bulks. Biosyst. Eng. 94, 545–555. https://doi.org/10.1016/j.biosystemseng.2006.04.013.

Nyström, I., Udupa, J.K., Grevera, G.J., Hirsch, B., 2002. Area of and volume enclosed by digital and triangulated surfaces, in: Proceedings of SPIE 4681- The International Society for Optical Engineering. pp. 669–680. https://doi.org/10.1117/12.466977.

Ortona, A., Pusterla, S., Fino, P., MacH, F.R.A., Delgado, A., Biamino, S., 2010. Aging of reticulated Si-SiC foams in porous burners. Adv. Appl. Ceram. 109, 246–251. https://doi.org/10.1179/174367510X12663198542586.

N. Otsu A Threshold Selection Method from Gray-Level Histograms. IEEE Trans. Syst. Man Cybern. Syst. smc-9 1979 62 66 https://doi.org/0018-9472/79/0100-0062 $00.75.

Ou, X., Zhang, X., Lowe, T., Blanc, R., Rad, M.N., Wang, Y., Batail, N., Pham, C., Shokri, N., Garforth, A., Withers, P., Fan, X., 2017. X-ray micro computed tomography characterization of cellular SiC foams for their applications in chemical engineering. Mater. Charact. 123, 20–28. https://doi.org/10.1016/j.matchar.2016.11.013.

Ozmat, B., Leyda, B., Benson, B., 2004. Thermal applications of open-cell metal foams. Mater. Manuf. Process. 19, 839–862. https://doi.org/10.1081/lmmp-200030568.

Palma, V., Pisano, D., Martino, M., 2018. Comparative study between aluminum monolith and foam as carriers for the intensification of the CO water gas shift process. Catalysts 8. https://doi.org/10.3390/catal8110489.

Papetti, V., Dimopoulos Eggenschwiler, P., Della Torre, A., Lucci, F., Ortona, A., Montenegro, G., 2018. Additive manufactured open cell polyhedral structures as substrates for automotive catalysts. Int. J. Heat Mass Transf. 126, 1035–1047. https://doi.org/10.1016/j.ijheatmasstransfer.2018.06.061.

Petit, C., Maire, E., Meille, S., Adrien, J., 2017. Two-scale study of the fracture of an aluminum foam by X-ray tomography and finite element modeling. Mater. Des. 120, 117–127. https://doi.org/10.1016/j.matdes.2017.02.009.

Plateau, J., 1873. Experimental and Theoretical Statics of Liquids Subject to Molecular Forces Only, Volume 1. Gauthier-Villars, Paris.

Plumb, J.C., Lind, J.F., Tucker, J.C., Kelley, R., Spear, A.D., 2018. Three-dimensional grain mapping of open-cell metallic foam by integrating synthetic data with experimental data from high-energy X-ray diffraction microscopy. Mater. Charact. 144, 448–460. https://doi.org/10.1016/j.matchar.2018.07.031.

Poco, J.F., Satcher, J.H., Hrubesh, L.W., 2001. Synthesis of high porosity, monolithic alumina aerogels. J. Non. Cryst. Solids 285, 57–63. https://doi.org/10.1016/S0022-3093(01)00432-X.

Podio-Guidugli, P., Favata, A., 2014. Elasticity for Geotechnicians. Solid Mech. its Appl. 204, 149–157. https://doi.org/10.1007/978-3-319-01258-2.

Poryles, R., Gland, N., King, A., Rosenberg, E., Barré, L., Chevalier, T., 2020. Foam trapping in a 3D porous medium: in situ observations by ultra-fast X-ray microtomography. Soft Matter 16, 6354–6361. https://doi.org/10.1039/d0sm00392a.

Randrianalisoa, J., Baillis, D., Martin, C.L., Dendievel, R., Roberts, A.P., Garboczi, E.J., 2002. Microstructure effects on thermal conductivity of open-cell foams generated from the Laguerre-Voronoï tessellation method. J. Mech. Phys. Solids 50, 33–55. https://doi.org/10.1016/j.ijthermalsci.2015.07.016.

Razza, S., Heidig, T., Bianchi, E., Groppi, G., Schwieger, W., Tronconi, E., Freund, H., 2016. Heat transfer performance of structured catalytic reactors packed with metal foam supports: influence of wall coupling. Catal. Today 273, 187–195. https://doi.org/10.1016/j.cattod.2016.02.058.

Richard Ketcham, n.d. X-ray Computed Tomography (CT) [WWW Document]. URL https://serc.carleton.edu/research_education/geochemsheets/techniques/CT.html (accessed 2.12.21).

Richardson, J.T., Peng, Y., Remue, D., 2000. Properties of ceramic foam catalyst supports: pressure drop. Appl. Catal. A Gen. 204, 19–32. https://doi.org/10.1016/S0926-860X(00)00508-1.

Richardson, J.T., Remue, D., Hung, J.K., 2003. Properties of ceramic foam catalyst supports: mass and heat transfer. Appl. Catal. A Gen. 250, 319–329. https://doi.org/10.1016/S0926-860X(03)00287-4.

T.W. Ridler S. Calvard Picture Thresholding Using an Iterative Selection Method IEEE Trans. Syst. Man Cybern. smc-8 1978 630 632 https://doi.org/0018-9472/78/0800-0632$00.75.

Scheffler, M., Colombo, P., 2005. Cellular Ceramics: Structure, Manufacturing, Properties and Applications. WILEY-VCH Verlag GmbH & Co. KGaA, Weinheim.

Schlegel, A., Benz, P., Buser, S., 1993. Wärmeübertragung und Druckabfall in keramischen Schaumstrukturen bei erzwungener Strömung. Wärme- und Stoffübertragung 28, 259–266. https://doi.org/10.1007/BF01539491.

Schmierer, E.N., Razani, A., 2006. Self-consistent open-celled metal foam model for thermal applications. ASME J. Heat Mass Transf. 128, 1194–1203. https://doi.org/10.1115/1.2352787.

Schmierer, E.N., Razani, A., Keating, S., Melton, T., 2016. Characterization of high porosity open-celled metal foam using computed tomography. ASME Int. Mech. Eng. Congr. Expo. 1–10.

Shimizu, T., Matsuura, K., Furue, H., Matsuzak, K., 2013. Thermal conductivity of high porosity alumina refractory bricks made by a slurry gelation and foaming method. J. Eur. Ceram. Soc. 33, 3429–3435. https://doi.org/10.1016/j.jeurceramsoc.2013.07.001.

Sinn, C., Wentrup, J., Pesch, G.R., Thöming, J., 2021. Heat transport in open-cell foams: CFD analysis of artificial heat sources vs fully resolved exothermal reactions. Ind. Eng. Chem. Res. 60, 4542–4551. https://doi.org/10.1021/acs.iecr.0c05982.

Specchia, S., Ercolino, G., Karimi, S., Italiano, C., Vita, A., 2017. Solution combustion synthesis for preparation of structured catalysts: A mini-review on process intensification for energy applications and pollution control. Int. J. Self-Propagating High-Temperature Synth. 26, 166–186. https://doi.org/10.3103/S1061386217030062.

Thomson (Lord Kelvin), W., 1887. On the division of space with minimum partition area. Philos. Mag. Lett. 24, 503–514.

Tseng, C.-J., Tsai, B.T., Liu, Z.-S., Cheng, T.-C., Chang, W.-C., Lo, S.-K., 2012. A PEM fuel cell with metal foam as flow distributor. Energy Convers Manag 62, 14–21. https://doi.org/10.1016/j.enconman.2012.03.018.

Twigg, M.V., Richardson, J.T., 2002. Theory and applications of ceramic foam catalysts. Chem. Eng. Res. Des. 80, 183–189. https://doi.org/10.1016/S0263-8762(02)72166-7.

Twigg, M.V., Richardson, J.T., 2007. Fundamentals and applications of structured ceramic foam catalysts. Ind. Eng. Chem. Res. 46, 4166–4177. https://doi.org/10.1021/ie061122o.

Vazifeshenas, Y., Sedighi, K., Shakeri, M., 2020. open cell metal foam as extended coolant surface – fuel cell application. Fuel Cells 20, 108–115. https://doi.org/10.1002/fuce.201800147.

Vicente, J., Topin, F., Daurelle, J.V., 2006. Open celled material structural properties measurement: from morphology to transport properties. Mater. Trans. 47, 2195–2202. https://doi.org/10.2320/matertrans.47.2195.

Visconti, C.G., Groppi, G., Tronconi, E., 2013. Accurate prediction of the effective radial conductivity of highly conductive honeycomb monoliths with square channels. Chem. Eng. J. 223, 224–230. https://doi.org/10.1016/j.cej.2013.02.095.

Visiocell® | Recticel Flexible Foams [WWW Document], n.d. . Visiocell® Innov. accuracy. URL https://recticelflexiblefoams.com/consumergoods/visiocell (accessed 3.8.21).

Weaire, D., Phelan, R., 1994. A counter-example to kelvin's conjecture on minimal surfaces. Philos. Mag. Lett. 69, 107–110. https://doi.org/10.1080/09500839408241577.

Wejrzanowski, T., Skibinski, J., Szumbarski, J., Kurzydlowski, K.J., 2013. Structure of foams modeled by Laguerre-Voronoi tessellations. Comput. Mater. Sci. 67, 216–221. https://doi.org/10.1016/j.commatsci.2012.08.046.

Zalucky, J., Möller, F., Schubert, M., Hampel, U., 2015. Flow regime transition in open-cell solid foam packed reactors: adaption of the relative permeability concept and experimental validation. Ind. Eng. Chem. Res. 54, 9708–9721. https://doi.org/10.1021/acs.iecr.5b02233.

Zheng, Y., Luo, X., You, J., Peng, Z., Zhang, S., 2020. Ceramic foams with highly open channel structure from direct foaming method in combination with hollow spheres as pore-former. J. Asian Ceram. Soc. 1–11 https://doi.org/10.1080/21870764.2020.1847427.